A15 STOICHIOMETRY AND GRAIN MORPHOLOGY IN ROD-IN-TUBE AND TUBE TYPE Nb_3Sn STRANDS; INFLUENCE OF STRAND DESIGN, HEAT TREATMENTS AND TERNARY ADDITIONS

Thesis

Presented in Partial Fulfillment of the Requirements for the Degree Master of Science in the Graduate School at The Ohio State University

By

Shobhit Bhartiya, B.Tech

Graduate Program in Materials Science and Engineering

The Ohio State University

2010

Thesis Committee:

Professor Michael Sumption, Advisor

Professor John Morral, Advisor

Professor Katharine Flores

ABSTRACT

In the present work multifilamentary Tube type and distributed barrier Rod-in-Tube (RIT) type Nb_3Sn composites were studied in detail. Tube type composites consisting of subelements of Nb-7.5 wt% Ta alloys with simple Cu/Sn binary metal inserts were studied in an attempt to enhance the performance boundaries of these conductors. We focused on correlating the composition and morphology of the intermetallic A15 to the transport and magnetic properties for varying heat treatments. In particular, lower temperature HTs were studied, specifically 625°C and 635°C as a function of time. The extent of A15 formation, the ratio of the coarse/fine grain areas, and the amount of untransformed 6:5 phase were then observed as a function of time –temperature.

A15 stoichiometry was investigated and compared for two different Nb_3Sn strand designs, specifically Tube type and high performance RIT type strands. Transport measurements were performed on both categories of conductors for various conditions. The objective of the study was to

investigate the limits of tube type conductor performance and to compare this to that of RIT conductors. Specifically, the Sn stoichiometry and A15 grain size for RIT and Tube type conductors were compared and to correlated with the transport properties of the two strand types. Tube type conductors were compared to RIT conductors, each after the application of single step and two-step HTs with plateaus ranging from 615°C to 675°C for various times. The influence of strand geometry and reaction route was related to the resulting A15 stoichiometries. Fractography was performed to investigate the effect of a two-step reaction on the morphology, the ratio of coarse/fine grain area and grain size of fine grain A15. The effect of Ti doping on superconducting properties of RIT type Nb_3Sn strands was also studied.

ACKNOWLEDGEMENTS

I have numerous people to thank for making my time at the Center for Superconducting and Magnetic Materials (CSMM) a pleasant and productive one. Foremost, I must thank my advisor, Dr. Michael Sumption, for his guidance, understanding and patience with this thesis work.

I am deeply indebted to my co-advisor, Dr. John Morral for his advice and constructive comments which have been valuable for me. I also wish my sincere thanks to Dr. Edward W. Collings for his invaluable comments and insights throughout the work.

I would like to thank to Michael Tomsic (HyperTech Research Inc.), Eric Gregory (Supergenics LLC) and Xuan Peng (Global Research Inc.) for providing superconducting samples examined in this work. I am grateful to X. Peng for sharing her knowledge on the subject and detailed explanation of manufacturing process. I appreciate her help for heat treatments of the

samples for electron microscopy studies. I am also thankful for her help and suggestions regarding my future career.

I am thankful to the technical staff in the Materials Science and Engineering Department at The Ohio State University especially, Cameron Begg, Steve Bright and Henk Colijn for their assistance in sample preparation and electron microscopy.

I thank my fellow graduate students Mohammad Mahmud, Michael Susner, Vishal Ryan Nazareth, and Scott Bohnenstiehl, for making my life at CSMM an enjoyable one.

Lastly, and most importantly, I would like to thank my parents and family member for their motivation, love and constant support throughout my endeavors without which I would not be where I am.

VITA

August 29, 1982……..…Born- Kanpur, India

2002-2006…….……...B.Tech,
Institute of Technology, Banaras Hindu University (IT-BHU), India

2007-2009…….....Graduate Research Associate
Center for Superconducting and Magnetic Materials (CSMM)
The Ohio State University, USA

FIELDS OF STUDY

Major Field: Materials Science and Engineering

CONTENTS

Page

LIST OF TABLES

LIST OF FIGURES

Figure Page

CHAPTER 1

INTRODUCTION

1.1 Introduction to Nb_3Sn and its Place in Superconducting Materials

Superconductivity in Nb_3Sn was observed by Matthias et al in 1954 [1], after the first superconductor V_3Si with A15 structure was discovered by Hardy and Hulm in 1953 [2]. Nb_3Sn has the capacity to carry high current as compared to the commonly used NbTi and therefore is a very important material for high field applications. Nb_3Sn has a higher upper critical field (B_{c2}) and critical temperature (T_c) than NbTi based alloys (~25 T [3] and 18.3 K [4] for binary Nb_3Sn versus ~ 15.4 T [5] and 9.3 K [6] for NbTi (B_{c2} values are at 0 K)). Extensive research has been carried out to improve the performance of these conductors. Efforts over the past decade have resulted in a substantial increase in the critical current density of Nb_3Sn superconducting wires as shown by Parrell et al [7].

As will be discussed in detail in Chapter 2, Nb_3Sn composites are fabricated by a variety of process including the bronze route, Rod-In-Tube route, Powder-in-Tube (PIT) route, and the Tube Type method. All of these

methods follow a two-step approach in the formation of the brittle Nb_3Sn phase. In the first step these composites are fabricated by number of different processes like wire drawing and extrusion. The next step involves the heat treatment of these composites to form A15 phase by reactive diffusion of Sn atoms with Nb. Beyond this basic similarity, the processes vary substantially in their details, as well as the materials science based processes which are associated with them. Presently, the Nb_3Sn strand with the highest critical current density (J_c) is made by the Rod-In-Tube, distributed barrier process, with transport J_c values beyond 3000 A/mm^2 at 12 T, 4.2 K [8].

The main focus of the development of Nb_3Sn conductors is the production of cost effective magnets with high performance [9]. A detailed understanding of the phase formation during heat treatment as well as the effects of the final microstructure on the superconducting properties is necessary to achieve high J_c and B_{c2}. This would enable tailoring the microstructure to obtain the desired properties. One of the main challenges related to enhancing the performance of Nb_3Sn includes increasing the Sn content to attain a more stoichiometric Nb_3Sn A15 phase. The refinement of grain size is also important, as reductions in grain size increase grain boundary pinning, thereby increasing critical current density.

1.2 Short Introduction to Superconductivity

Superconductivity is the state which is reached in some materials at lower temperatures, is commonly identified by the absence of electrical resistance. This phenomenon was first observed by Kamerlingh Onnes in 1911 [10] after he was successful in liquefaction of Helium. He demonstrated that DC electrical resistivity disappeared when mercury was cooled below critical temperature of about 4.2 K. A schematic superconducting transition is illustrated in (Fig. 1.1).

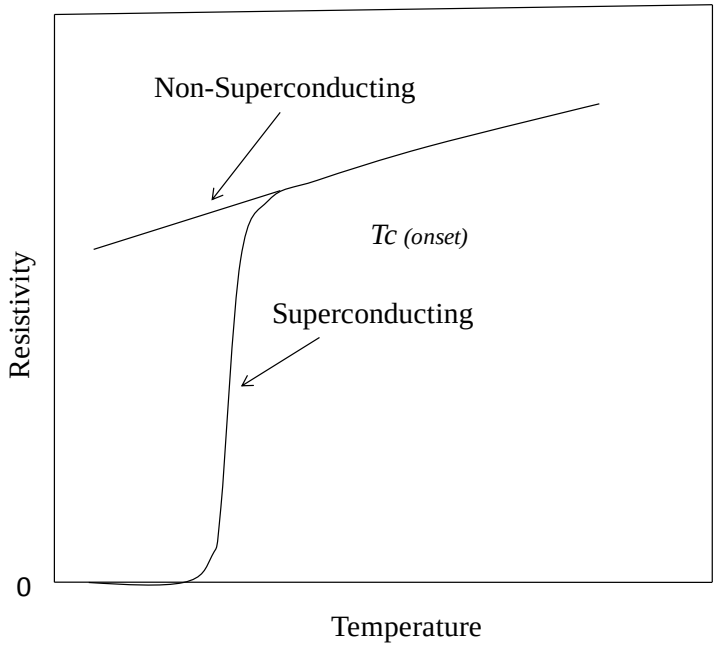

Fig. 1.1 Illustration of sudden drop to zero resistivity in a superconducting material, as compared to a non-superconducting sample.

There are three critical parameters that determine whether a superconductor will be in its normal (resistive) state or the superconducting state. These are current density (J), magnetic field (B) and temperature (T). These parameters plotted in a 3-D space give a surface beneath which given material is in the superconducting state. Any region outside this surface is normal (i.e. resistive) for a given material. Such a surface is called critical surface and the upper limits for these parameters are the critical temperature (T_c), critical magnetic field (B_c), and critical current density (J_c). Critical current density (J_c) is defined as the maximum resistance-less current (I_c) per unit cross sectional area of the superconducting wire. Note that here and throughout the text we use SI units, and that the external field, the magnetic field strength, is denoted H, while inside the superconductor, the magnetic induction is given by $B = \mu_0(H+M)$ where μ_0 is the permeability of free space and M is the magnetization of the superconductor. For convenience in units we will sometimes refer to $\mu_0 H$ in tesla.

The phenomenon of superconductivity exists in number of metals and alloys with the exception of noble and ferromagnetic materials. In the presence of an external magnetic field (H) superconductors can be classified into two types; Type I and Type II. Type I superconductivity is associated

with nearly all the elemental superconductors. In Type I superconductivity, magnetic flux is perfectly excluded from the interior of the superconductor (this is the Meissner effect). It takes place up to a critical field H_c. It is important to note that for the Meissner effect it is flux, and not the change in flux, which is shielded from the superconductor, in particular flux is expelled from the superconductor as it is cooled through T_c, which would not be the case for a "simple" state of perfect conductivity. The magnetic field exponentially decays from the surface of the superconductor over a magnetic penetration depth λ. For fields above $H_{c,}$ complete penetration of magnetic flux takes place and superconductivity is lost.

Type II superconductors only exhibit perfect magnetic flux exclusion up to a lower critical field H_{c1} ($H_{c1} << H_{c2}$). At H_{c1}, magnetic flux penetrates in the superconductor in the form of quantized flux vortices or fluxons and the superconductor is said to be in a mixed state. At much higher fields, the upper critical field (H_{c2}) is reached and the superconductor becomes normal.

Another fundamental superconducting property is the pairing of electrons to form Cooper pairs which is due to electron-phonon interaction (for BCS superconductors like Nb_3Sn). This property allows the resistance-free flow of electron pairs. The distance between the pairs of electron is the

coherence length (ξ). In stoichiometric Nb_3Sn superconductor ξ and λ are about 3 nm and 60 nm respectively [11].

As mentioned above superconducting material is penetrated by fluxons when the applied field greater than H_{c1}. These flux-lines form a lattice of normal conducting region with the approximate diameter of two times the superconducting coherence length ξ. The superconducting bulk is shielded from these normal regions by supercurrents encompassing the cores of each of the fluxones individually, with a screening depth between the core and the bulk of λ.

As the applied magnetic field is increased above H_{c1}, the flux density B, starting from zero, increases until the field reach B_{c2}. At B_{c2} the flux-lines starts to overlap ($B_{c2} = \mu_o H_{c2}$) and superconductivity is extinguished. When a transport current flows through a superconductor, a Lorentz force

$$F_L = J \, X \, B \tag{1.1}$$

acts perpendicular to both applied field and the current on the fluxons. Movement of the flux-lines will result in dissipation of energy and destroy the zero resistivity state. In real materials, the fluxons are prevented to from moving (pinned) by lattice imperfections such as impurities, defects, or grain boundaries. Thus in order to have loss-less current in the presence of

magnetic fields, fluxon pinning is essential. Critical current density is reached when the Lorentz force F_L becomes greater than the pinning force F_P that binds the fluxon. Therefore, the first voltage encountered during J_c measurement is that of the fluxon motion, rather than a total and abrupt change to the normal or resistive state. Looking back to Figure 1, the initial transition from a zero resistance to some non-zero resistance with increasing field describes the initial fluxon motion in a type II superconductor.

The field at which $F_P = 0$ is H_{irr} (irreversibility field) and no bulk super current can flow above this field. The condition $F_P = 0$ yields the maximum magnetic field of usefulness for the superconductor which is an important materials parameter. Looking back to again to Figure 1.1, the temperature at which transition from the normal to the superconducting state begins ($T_{c(onset)}$) corresponds to H_{c2}. while the temperature where resistivity becomes zero ($T_{c\ (min)}$ or T_{irr}) , is related to H_{irr}.

A15 Nb-Sn behaves as a Type II superconductor. Its current carrying capability for any practical field thus relies on its capability to pin the flux lines. The bulk pinning is given by the equation:

$$F_P \equiv - J_c X B \qquad (1.2)$$

The bulk pinning force depends on magnetic field and the field value at which force is maximum depends on flux-line to lattice interaction [12-15]. Equation 1.2 indicates that the pinning force determines the conductor's current carrying capacity. It is known that the grain boundaries in the A15 phase represents the primary pinning centers for Nb_3Sn. This is supported by strong experimental evidence in which maximum pinning force is related to the reciprocal of grain size [16-20].

Achieving high critical current density requires that the A15 grains be kept small, approximately less than 200 nm. A small grain size requires a low Nb_3Sn reaction temperature [16] which is not favorable to attain high Sn-content, resulting in depressed H_{c2} [21] and T_c values. Growing large, stoichiometric Nb_3Sn layers and at the same time maintaining a fine grain size has been an inherent challenge in processing Nb_3Sn superconductors, and this is a significant theme of this thesis.

1.3 Scope of the Thesis

Multifilamentary Tube type and distributed barrier RIT type Nb_3Sn strands were studied in detail in the present work. Transport measurements were performed on both categories of the conductors under various conditions. The main focus of work was to investigate the limits of Tube type conductor performance and to compare them to those of RIT conductors. Specifically, the route was to compare the Sn stoichiometry and A15 grain sizes for RIT and Tube Type conductors and to correlate the results with differences in transport properties of two strand types. The influence of strand design and dopant additions on the performance of conductors was also studied. In addition to the above, the effects of various heat treatments on microstructure and properties of Nb_3Sn were also studied. The purpose was to attain fine grain size with maximal Sn content.

In Chapter 4, we focused on correlating the composition and morphology of the intermetallic A15 to the transport and magnetic properties for varying heat treatments. In particular, lower temperature HTs were studied, specifically 625°C and 635°C for various times. The extent of A15, the ratio of the coarse/fine grain areas, and amount of the untransformed 6:5 phase were then observed as a function of time –

temperature. Compositional analysis was carried out on the A15 phase to study the variation in stoichiometry as a function of temperature. Fractography was also performed to investigate the effect of temperature and alloying on the morphology and grain size of the fine grain A15.

Chapter 5 deals with the investigation and comparison of A15 stoichiometry for two different Nb_3Sn strand designs, Tube Type and high-performance, distributed-barrier RIT type. The focus of the study was to attain fine grain A15 with maximal Sn stoichiometry. Tube type conductors were compared to RIT conductors, after the application of single step and two-step HTs with plateaus ranging from 615°C to 675°C for various times. The influence of strand geometry and reaction route was related to the resulting A15 stoichiometries. Short sections of strand were encapsulated and then reacted, after which SEM (BSE) and EDS were used to observe the structures and obtain Sn concentration profiles. Fractography was performed to investigate the effect of a two-step reaction on the morphology, the ratio of coarse/fine grain area and grain size of fine grain A15. The influence of Ti doping on superconducting properties of RIT type Nb_3Sn strands was also studied.

All of this is then discussed in the concluding chapter, Chapter 6, were we show that the main reason for the difference in RIT and Tube type conductor performance is associated with conductor area utilization, and suggest methods for increasing Tube conductor performance.

CHAPTER 2

Nb_3Sn SUPERCONDUCTORS

2.1 Introduction

Out of a wide range of superconducting materials including pure metals, alloys, compounds, oxides and inorganic materials, Nb_3Sn is one of the most practical materials for high field application. While a number of other superconducting A15 compounds exist, Nb_3Sn is preferred because of a combination of good properties and ease of fabrication compared to other A15 compounds. Specifically Nb_3Sn is preferred for emerging High Energy Physics applications which require operation at high fields. The properties of intermetallic Nb_3Sn are discussed in the following sections.

2.2 Properties of Nb_3Sn

2.2.1 Crystal Structure

Nb_3Sn possess the brittle A15 crystal structure. For a generic A15 compound, A_3B, the "B" atoms reside on a body-centered cubic lattice with two "A" atoms on each face (Fig. 2.1).

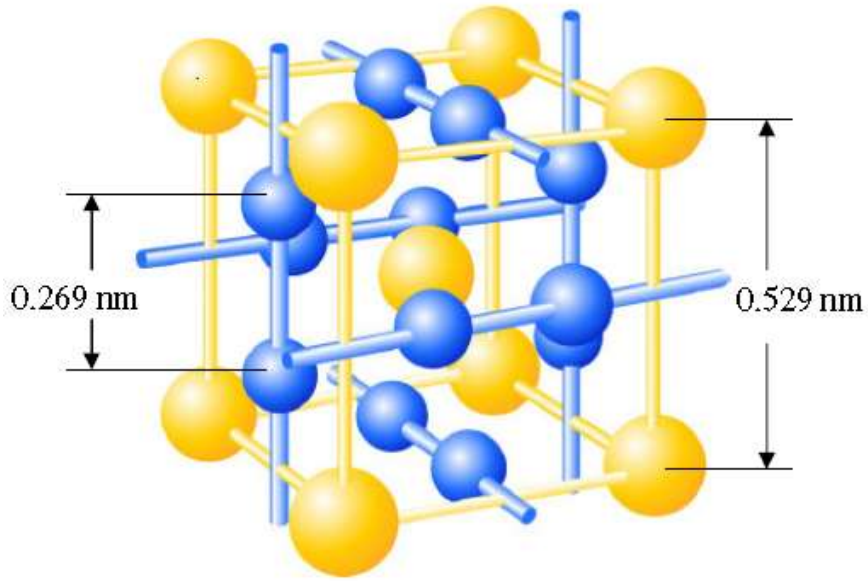

Fig. 2.1 Atomic arrangement of generic A15 compound. B atoms (yellow) occupy BCC lattice sites while "A" (blue) atoms are in the form of orthogonal chains through the face centers, after Godeke [22].

Forty-six A15 compounds are known to be superconducting, niobium and vanadium compounds generating the highest T_c values. The excellent superconducting properties found in A15's are attributed to the close distance of the Nb or V atoms and to the high degree of order in stoichiometric composition. The A15 lattice parameter of the A15 is 0.529 nm at the stoichiometric composition and the spacing between the Nb atoms in the A15 is around 0.265 nm which is less than that in elemental Nb (0.290 nm) [23]. As a result it possesses increase density of states giving better superconducting properties compared to *bcc* Nb [22].

2.2.2 The Niobium-Tin (Nb_3Sn) Phase Diagram

The Nb-Sn phase diagram as determined by Charlesworth *et. al.* [24] is the generally accepted phase diagram and is shown in the Fig. 2.2. The Nb-Sn system consists of three intermetallic phases $NbSn_2$, Nb_6Sn_5 and Nb_3Sn. In the Charlesworth Nb_3Sn phase diagram, the composition over which Nb_3Sn phase is stable varies from approximately 18% to 25% and is relatively constant (with temperature range from 0 to 1675°C), unlike proposed Nb_3Sn phase diagrams [25, 26], where the composition range vary more strongly with temperature. The A15 phase is the only superconducting phase.

Stoichiometric Nb_3Sn has T_c of 18.3 K, however T_c diminishes with decreasing Sn composition, to a value of 6 K at the Sn-poor side of the Nb_3Sn phase. A cubic to tetragonal phase transformation occurs at lower temperature (T < 43 K) for the composition above 24.5 at.% Sn, degrading the superconducting properties (density of states decreases).

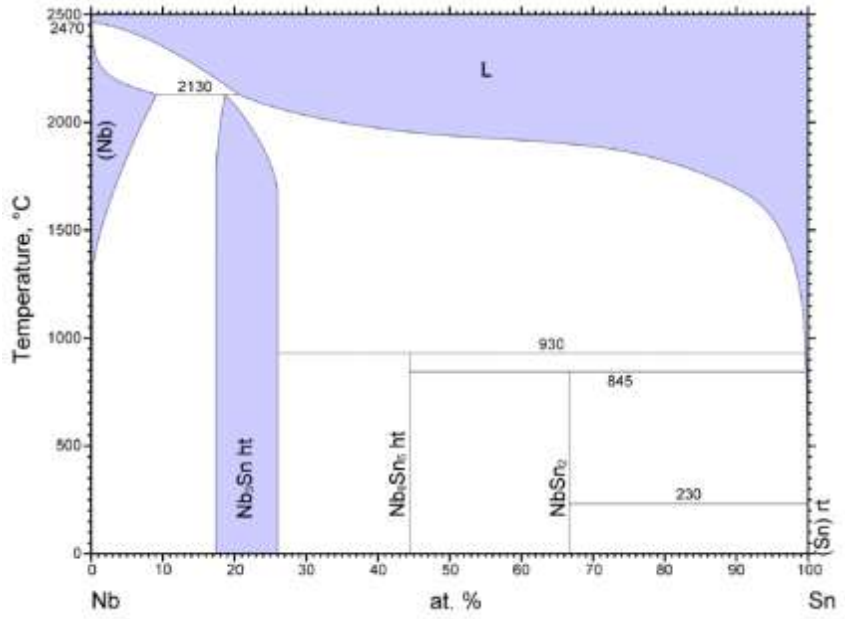

Fig. 2.2 Nb-Sn binary phase diagram determined by Charlesworth *et. al.* [24] (Reprinted with permission of ASM international).

2.2.3 T_c and H_{c2} as a the Function of Atomic Sn Content

As seen in the phase diagram (Fig. 2.2) the Nb_3Sn A15 phase is stable in the range of 18-25 at.% Sn, therefore it is important to know the variation of the T_c and $B_{c2} = \mu_0 H_{c2}$ with composition. Equation (2.1) and (2.2) summarize the data from the work of Devantay *et al.* [23] and Godeke [22] for the variation of T_c and H_{c2} as function of at.% Sn (β). As seen from Equation (2.1), from Godeke [22]

$$T_c(\beta) = \frac{-12.3}{1+\exp\left(\frac{\beta-0.22}{0.009}\right)} + 18.3 \quad (2.1)$$

T_c increases with an increase in Sn stoichiometry, assuming a maximum of 18.3 K, the highest recorded value for Nb_3Sn [27].

Also from Godeke [22], we find Equation (2.2), where

$$\mu_\circ H_{c2}(\beta) = -10^{-30}\left(\frac{\beta}{0.00348}\right) + 577\beta - 107 \quad (2.2)$$

is the summation of an exponential and a linear fit, shows increase in H_{c2} with the increase in the Sn content up to 24.5 at% Sn and above that it starts decreasing due to the cubic to tetragonal phase transformation. Thus, to attain best superconductive properties, a homogeneous and stoichiometric Nb_3Sn phase is desired.

2.2.4 Copper, Tantalum, and Titanium Additions to Nb_3Sn

The presence of copper lowers the A15 formation temperature, thereby limiting the grain growth and thus retaining a higher grain boundary density required for pinning. Copper is present in elemental form in RIT, PIT, and Tube Type strands while in the Bronze process the Cu is present as a Cu-Sn alloy. In all cases Cu-Sn phases act as the Sn source to form the

A15. It has also been found that the presence of Cu destabilizes line compounds such as $NbSn_2$ and Nb_6Sn_5 during A15 formation. Although Cu can be detected in the A15 layers, it is generally assumed to exist only at the grain boundaries and not to appear in the A15 grains [28]. Finally, the presence of copper was recently suggested to lead to possible B_{c2} suppression in wires.

The performance of Nb_3Sn superconductors can be enhanced by the addition of titanium and tantalum. Past studies on the doping of Nb-Sn with ternary elements suggest Ti and Ta as the most effective additions for the enhancement of J_c and B_{c2}. While Ta is usually added as an alloying addition in the Nb filament, Ti is added in several different ways, the most common of which is in the form of a Sn-Ti alloy. Both Ti and Ta occupy Nb sites in the A15 lattice and have been found to suppress the cubic to martensitic transformation. Retention of the cubic phase results in an increase in B_{c2}. In addition to the above, both Ta and Ti have been found to increase the normal-state resistivity and in turn increase B_{c2}.

Small additions of Ti significantly enhance J_c at very high fields ($H >$ 16 A/m) and reduce it at lower fields. The usual explanation for this is Ti tend to increase B_{c2}, thus increasing high field J_c. This makes Ti additions

particularly desirable for construction of magnets to produce very high fields (>20 T). On the other hand, Ta additions are known to enhance high field J_c and the low field J_c at the same time. The usual explanation for this is an increase in B_{c2} (increasing high field J_c) and refinement of grain size, enhancing flux pinning which increases low field J_c as well. Also Ti increases the layer growth rate, thereby forming A15 at smaller reaction times [29].

2.3 Multifilamentary Wire Fabrication Techniques

Applications using Nb_3Sn wires generally require the A15 to be embedded in a normal conducting matrix for electrical and thermal stability reasons. Since the A15 phase is brittle the wires are drawn while the components are not yet reacted to the A15 phase and remain ductile. The most commonly used fabrication methods are discussed below.

2.3.1 The Bronze Process

The Bronze process was the first viable wire fabrication process [30]. During assembly Nb rods are inserted in a high Sn bronze matrix which is surrounded by stabilization copper. After assembly this billet is then

extruded and drawn down to desired diameter. A schematic of wire cross-section is shown in the Fig. 2.3.

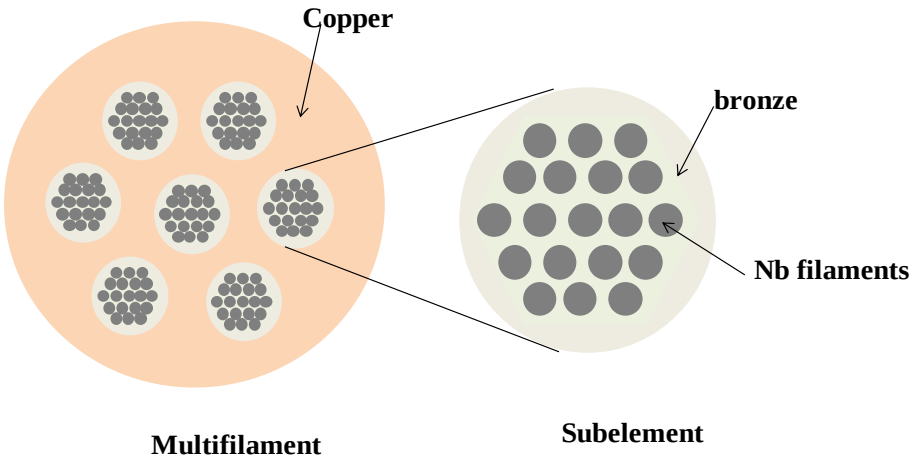

Fig. 2.3 Schematic of the wire drawn by Bronze Process.

In this process the A15 is formed via a solid state diffusion reaction between Nb and the bronze matrix. The subelements need to be surrounded by Nb or Ta barriers to prevent contamination of the Cu matrix with Sn during A15 formation. The main advantage of the process is the very fine filaments that it can make (≤ 5 microns) and a relatively straightforward wire fabrication.

However, the main drawback of the process is the work hardening of the bronze; therefore frequent annealing steps are required (after about every 50% area reduction). This makes the process more labor intensive and during annealing there can be some possibility of the formation of the Nb_3Sn phase, which hampers further wire drawing. Another drawback is the

limitation on the amount of Sn in the Cu matrix. The amount of Sn is limited by the maximum solubility of Sn in Cu (~9.1 at %). As a result a large Sn gradient is observed across the A15 due to a low Sn content in the bronze matrix [22] leading to low superconducting properties.

2.3.2 The Rod –In- Tube, Distributed Barrier Process

In the Rod-In-Tube (RIT) process [31] a Sn core is surrounded by Copper region embedded with Nb rods as shown in Fig. 2.4. These filamentary regions are surrounded by a Sn diffusion barrier (typically Nb or Nb (Ta)). The RIT process is advantageous compared to the bronze process because it allows wire processing to proceed to final size without intermediate anneals. During heat treatment the Sn atoms from the core diffuse through the Cu matrix and react with the Nb forming the A15 similar to the bronze conductors.

The other advantage of this process is the higher initial Sn/Cu ratio than the bronze route resulting in superior quality A15 region. The process has a number of drawbacks, perhaps the most important is the loss of Sn core region as A15 area and the interconnection of the filaments during A15 growth. These interconnections result in a large effective filament size of 70μm to 200μm. Another drawback is the longer heat treatment times due to

multiple pre-reaction steps required to form homogeneous Cu-Sn phases prior to A15 formation.

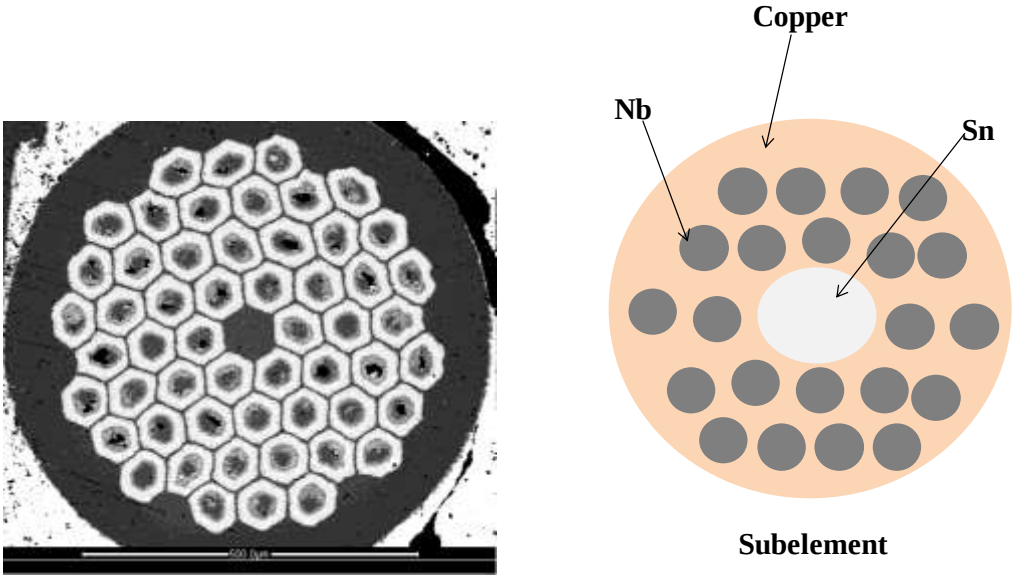

Fig. 2.4 Micrograph of the cross-section of the wire fabricated by Rod-in-Tube route (a schematic of the subelement is shown on the right side).

2.3.3 The Powder-in-Tube Process

In the powder-in-Tube (PIT) process [32], powders of $NbSn_2$ plus additional elements (typically Cu and Sn) are filled into Nb tubes which are embedded in a Cu matrix (Fig. 2.5). The main advantage of this process is the high Sn activity, resulting in short and low temperature reactions that limits the grain growth and small, well separated filaments. One of the

drawbacks is the non-ductility of the powder core making drawing difficult and resulting inhomogeneities in the strands. Another drawback of this type of conductor is the higher cost, as the Nb tubing and specialty powders are expensive, and it is difficult to control the powder size, which is crucial to the manufacturability of these conductors.

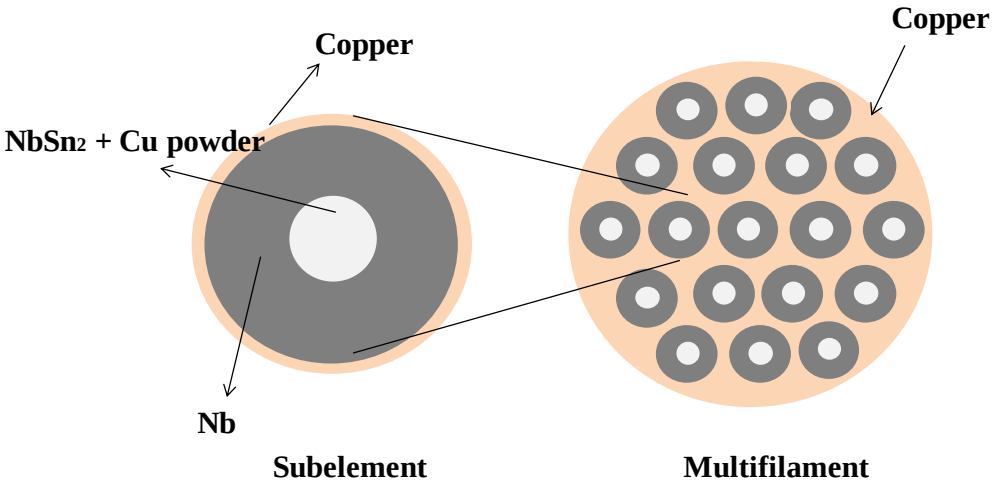

Fig. 2.5 Schematic of the wire drawn by Powder-in-Tube (PIT) Process.

2.3.4 The Tube-Type Process

To overcome the problems of the PIT process, a Tube Type method was developed [33]. In some ways the design is similar to PIT type; in these composites $NbSn_2$ powder core is replaced by pure Sn metal surrounded by thin tube of Cu as shown in Fig. 2.6. These composites have all the above

mentioned advantages of PIT strands [32, 34] along with an easier and cheaper fabrication process (wire drawing) due to the ductile Sn core.

During heat treatment the A15 forms via the $NbSn_2$ and Nb_6Sn_5 route by a liquid state diffusion reaction between the Nb filament and the Sn rich Cu-Sn alloy [35, 36]. Early on, geometrically similar conductors were fabricated by Murase and associates [37]. More recently several other groups have studied similar conductors, including Rodrigues [38] and Yamasaki [39, 40].

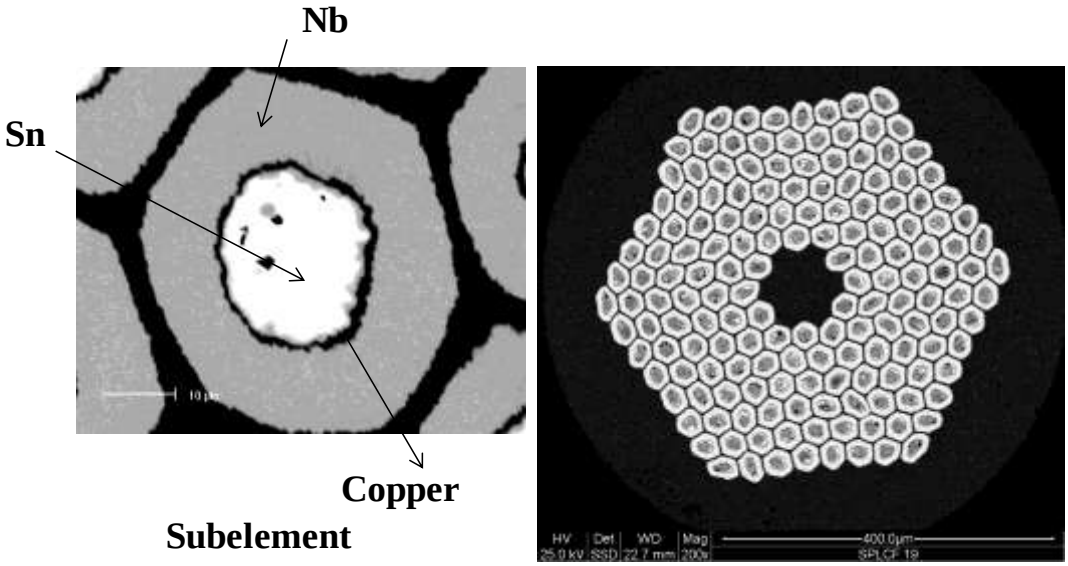

Fig. 2.6 BSE image of the cross-section of wire made by Tube Process.

Among all of the above processes, the Rod-In Tube method leads to the highest performance conductors (3000 A/mm^2 at 12 T and 4.2 K) and is the most commonly used for applications in high field magnets.

CHAPTER 3

EXPERIMENTAL PROCEDURES AND MEASUREMENT TECHNIQUES

3.1 Sample Specifications

For this thesis, there were two set of samples, a first set for low temperature reaction studies, and a second set for direct comparison studies. We will refer to the sets as the low temperature reaction set, and the direct comparison set; they are described in sections 3.1.1 and 3.1.2, respectively. Each set had its own series of heat treatments, these are described in sections 3.2.1 and 3.2.2.

3.1.1 Samples for Study of the Influence of Low Temperature Reaction Heat Treatments

The first set of samples, the low temperature reaction set, consisted of nine different Tube Type strands, which are described in Table 3.1. Strands S1-S5 had ODs of 0.75 mm while S6-S9 had ODs of 0.70 mm. These strand types where made with various numbers of subelements (from 61-217), and with various Cu-Nb-Sn ratios, but all had the same basic design. These strands were manufactured by HyperTech Research Inc. (Columbus, Ohio).

Representative strands are shown in Fig. 3.1, where we see backscatter electron (BSE) images of four strands S6-S9 in their unreacted state.

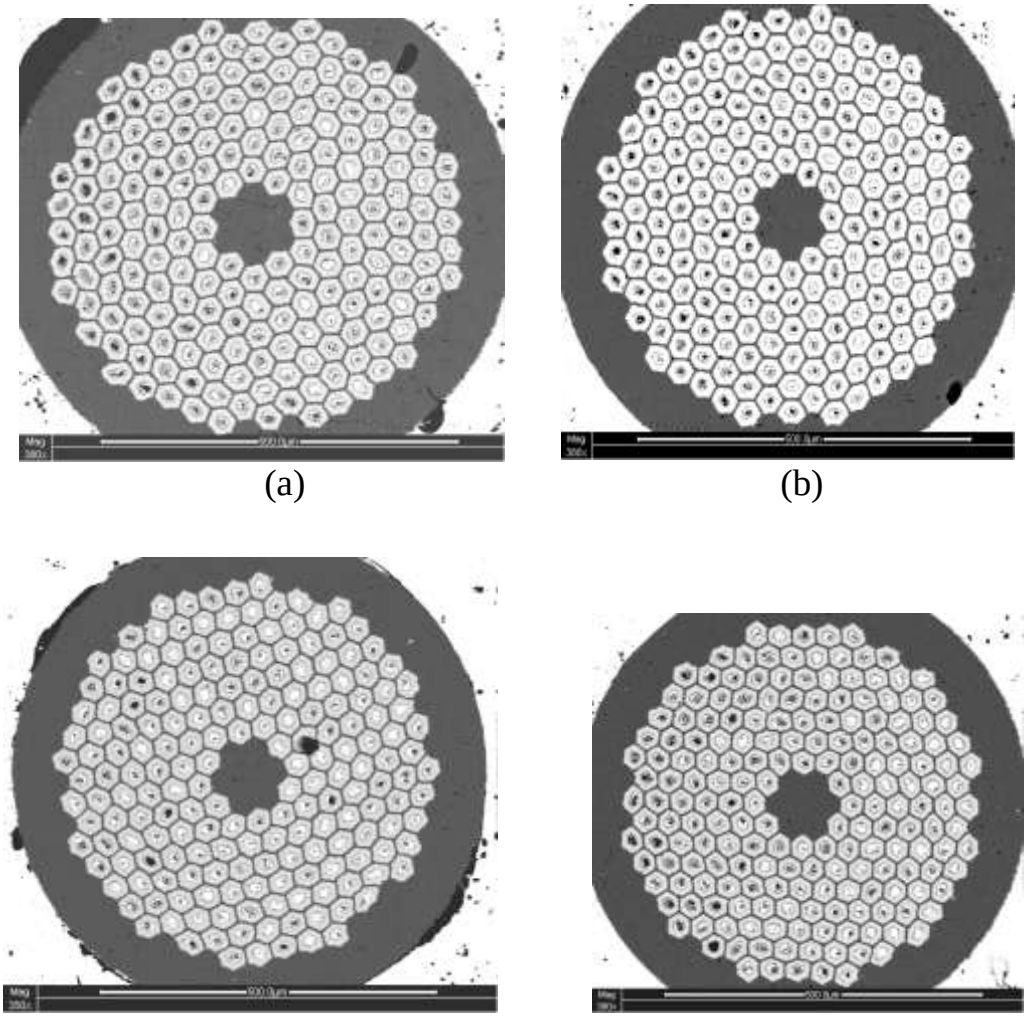

(a) (b)

(c) (d)

Fig. 3.1 BSE of overall strand for unreacted samples (a) S6, (b) S7, (c) S8, and (d) S9.

The Cu, Sn, Nb, and non-Cu areas of strands S1-S9 were determined by image analysis performed on SEM micrographs of fully deformed but

unreacted strands using Image tool software. This was done in preference to estimates on strands after assembly but prior to reduction, in order to correct for any differences in area reduction due to flow stress differences between the different metals in the strand. Listed in Table 3.1 are the resulting estimations of atomic fractions within the subelement for Cu, Sn, and Nb, denoted A_{Cu} at%, A_{Sn} at%, and A_{Nb} at%, respectively, as well as the area ratios with the subelement for Nb-to-Sn, $A_{Nb/Sn,}$ and Sn-to-Cu, $A_{Sn/Cu}$.

Strand	S1	S2	S3	S4	S5	S6	S7	S8	S9
No. Sub.	61	91	127	169	169	217	217	217	217
R_{sub} µm	28.5	23.8	20.6	15.3	17.9	--	---	---	---
A_{cu} at%*	6.4	6.1	4.02	3.77	2.95	4.35	5.2	6.05	2.78
A_{Sn} at%*	21.0	26.4	21.9	24.0	21.8	21.9	18.4	23.0	24.7
A_{Nb},at%*	72.0	67.5	74.1	72.2	75.2	73.7	76.4	70.9	72.5
$A_{Nb/Sn}$*	3.43	26	3.39	3.00	3.04	3.36	4.15	3.07	2.94
$A_{Sn/Cu}$ *	3.32	4.3	5.44	6.38	7.4	5.10	3.52	3.87	8.87

Table 3.1 Strand description (Tube Type) for low temperature reaction heat treatment study.

3.1.2 Samples for the Comparison of Transport Properties and A15 Microstructure for Tube Type and RIT Type Strands

The second set of samples, used for the direct comparison studies, consisted of two different strand types, Tube Type and distributed barrier RIT, described in Table 3.2 and Table 3.3 respectively. In this case all strands had an OD of 0.7 mm. Strands S6, S9 and S10 were Tube Type

strands and had subelement counts from 217 to 271, while R1, R2, R3, and GL1 were Rod-In-Tube strands with Subelement counts from 61 to 127. Listed in Table 3.3 are the atomic fractions within the subelement for Cu, Sn, and Nb, as well as the area ratios within the subelements for Nb-to-Sn and Sn-to-Cu. These values were based on area measurements performed on samples after the final wire drawing but before reaction.

Strand Name	**S6**	**S9**	**S10**
Number of subelements	217	217	271
Copper Area % (Subelement)	4.35	2.78	6.34
Tin Area % (Subelement)	21.9	24.67	23.26
Niobium Area % (Subelement)	73.7	72.5	70.40
Nb/Sn Area Ratio (Subelement)	3.36	2.94	3.00
Sn/Cu Area (Subelement)	5.03	8.87	3.67

Table 3.2 Strand description and parameters for Tube type samples for comparative study.

Strand Name	**R1**	**R2**	**R3**	**GL1**
Number of subelements	91	61	127	61
Copper Area % (Subelement)	15.76	-	-	15.76
Tin Area % (Subelement)	28.88	-	-	28.88
Niobium Area % (Subelement)	55.36	-	-	55.36
Nb/Sn Area Ratio (Sub.)	1.92	-	-	1.92
Ti % in the core	0	0	0	1.2

Table 3.3 Strand description and parameters for RIT type samples for comparative study.

3.2 Heat Treatment

For each set of samples, both the low temperature reaction sample set as well as the direct comparison set of samples, there were two distinct types of heat treatment sequences, these are described in detail below. Without regard to the specific HT sequence, there were two basic sample geometries into which samples were made for heat treatment; short straight samples and helical wires wound onto barrels. Short, straight samples were intended for electron optics study were 25 cm long (and the wire ends were sealed with a blowtorch) and were encapsulated in a quartz tube under 200 torr of Ar and heat treated in a tube furnace. The temperature ramp up was at a rate of 50°C/h, to a single or multiple temperature plateaus for various times. For

the J_c samples, an International Thermonuclear Experimental Reactor (ITER) barrel configuration was used. This is described more fully below, but is a helical length of wire about 1 m long mounted on a 3.2 cm diameter barrel for reaction and measurement. In order to heat treat under an inert atmosphere, the ITER barrel samples were heat treated under flowing Ar for various times.

3.2.1 Heat Treatments for the Study of the Influence of Low Temperature Reactions

Table 3.4 and 3.5 contains the specific heat treatment schedules intended for the study of influence of low temperature reaction heat treatments on the microstructure and properties of multifilamentary tube type Nb_3Sn strands. Two different HT series were used, the first for phase formation and reaction studies, the second for transport and electron optics studies of fully reacted strands. Table 3.4 gives the HT sequences for the phase formation and reaction studies, and Table 3.4 the HT sequences for the fully reacted strand studies. In both Table 3.4 and 3.5, some HT sequences included a pre–HT at 575°C for 48 h (indicated by P) followed by the reaction heat treatment. Strand S7 (with 23 at.% Sn) was chosen to

study the phase formation route in the Tube conductors when using low temperature reaction HTs. Because the idea was to look at the phase formation route in S6-S8, the HT sequences described in Table 3.4 were reactions for various times at the given reaction temperature. The various times gave samples with varying levels of reaction completeness, with the longest times giving fully reacted samples. A second series of HTs applied to the samples from the low temperature reaction studies were intended for investigation of the transport properties, stoichiometry, and microstructure of fully reacted strand, Table 3.5. The samples were given relatively full reaction heat treatments, although it was necessary to make sure that no or minimal Sn leakage was present into the matrix in order to be able to measure the transport properties properly.

Strand Name	Billet Name	HT(C/h)	Non-Cu%
S7	T1581	635/500,200,100,50,25,12,6,3,2,1 & 625/500,300,150,75,37,18,9,4,3,1	0.465

Table 3.4 Heat treatment sequences for phase formation and reaction studies

J_c HT	(S6) T1505 - 625°C/500h, 635°C/144h, 635°C/200h, P+635°C/300h (S7) T1581 - 635°C/200h (S9) T1628 - 635°C/250h, P+635°C/300h
EO HT	(S1) T1206 - 625°C/1000h (S2) T1102 - 625°C/1000h (S3) T1135 - 625°C/1000h (S4) T1162 - 625°C/1000h (S5) T1204 - 625°C/1000h

Table 3.5 Heat treatment for full reaction studies, intended for transport and electron optics measurements (HTs given as temperature/time).

3.2.2 Heat Treatments of Samples for the Comparison of Transport Properties and A15 Microstructures for Tube Type and RIT Type Strands

For the second sample set, the direct comparison set, there were two HT series. The first series contained reaction sequences with only a single step reaction, the second focused on two-step reactions; these series are listed in Tables 3.6 and 3.7, respectively. These tables list contain both Tube Type (S6, S9 and S10) and RIT type (R1-R3 and GL1) strands for the comparison of transport properties and A15 microstructure. Table 3.6 lists what are expected to be optimized single step reaction temperature/times for different strands. For the two-step HTs of Table 3.7 the focus of the heat treatment study was to attain fine grain A15 with maximal Sn stoichiometry.

Strand Name	Billet Name	Heat Treatment(C/h)	%Non-Copper
S6	T1505	625/500, 635/300	46.5
S9	T1628	625/300	46.5
S10	T1489	615/480	46.5
R1	EG36	650/50	49.5
R2	HP31	650/80	-
R3	EG36	650/40	-
GL1	EG36-Ti	625/56	49.5

Table 3.6 Sample reaction heat treatments for single step HT.

Strand Name	Billet Name	Heat Treatment(C/h)	%Non-Copper
S10	T1489	615/480,615/250+650/30, 615/250+650/70, 615/250+650/100, 615/250+650/120	46.50
R1	EG36	650/50, 625/130+675/30, 620/130+675/70, 625/130+675/100	49.50

Table 3.7 Sample reaction heat treatments for two-step HT.

3.3 Metallographic Sample Preparation for Electron Microscopy

The samples for electron microscopy were obtained from the central portions of the reacted strands (away from the pinched and fused ends, and in the center of the furnace hot zone). A hot mounting technique was used to prepare the sample. Wire samples (around 1.5 cm in length) were soldered onto a copper block, sectioned and conductive Bakelite powder was used to

form the mold. A Hot isostatic pressing technique was used to sinter the powder together. This results in a dense, conductive, and rigid mold.

The mounted samples were metallographically polished using SiC abrasive papers starting from 240 grit size up to 1200. They were then cleaned in ethyl alcohol using ultrasonic cleaning. Later they were mounted in stainless steel grips and polished for 6-10 hours in a vibratory polishing machine on one micron cloth using a silica gel colloidal solution. Prior to SEM analysis, final cleaning was done ultrasonically and then the sample was baked in an oven at 70°C for an hour. Fracture SEM samples were prepared by an etching technique in which samples were etched using a mixture of 0.1 N nitric acid for about 60 seconds. This was done to etch away the matrix Cu and obtain a brittle fracture surface for grain size analysis.

3.4 Critical Current Measurements

An ITER-barrel sample mount was used for the measurement of J_c. The ITER barrel is a helically grooved tube made up of Ti-6Al-4V alloy with grooved Cu rings attached at both ends. This is a modified design of the

sample holder as compared to the usual one, which had plane Cu rings. The unreacted wire was wound along the grooves under tension and was fixed by screws in the Cu end rings. The heat treatment of the barrel was performed in an inert atmosphere of argon. Prior to measurements (but after reaction) the ends of the wire were soldered onto the Cu end rings using Pb-Sn solder after which the barrel was mounted on the measuring probe. Care was taken to ensure that the barrel was well soldered to the probe to minimize the contact resistance. The voltage taps were soldered onto the sample with a gauge length of 30 cm between the taps.

After mounting the sample the probe is initially cooled in a liquid N_2 Dewar and then inserted into the bore of a superconducting magnet. The superconducting magnet can be ramped up to 15 T at liquid helium temperature (4.2 K). Current is passed through the sample, which is immersed in pool boiling helium and is exposed to various fields up to 15 T. The voltage across the sample is measured as a function of current at a particular field using four-point technique. In this technique a pair of twisted leads from the voltmeter was directly connected across the central portions of the sample while a separate leads were used to pass current through the sample.

3.5 SEM, EDS, and Image Analysis

In the scanning electron microscope (SEM), electrons are emitted from the cathode and accelerated towards the specimen surface. These electrons after striking the surface of the specimen scatter through the specimen within a defined volume called the interaction volume. Various signals including back scattered electrons (BSE), secondary electrons (SE), Auger electrons (AE) along with X-Rays are generated by electron beam-specimen interaction.

Back scattered electrons (BSE) are produced deep within the specimen and have much higher energy. The contrast in the image produced by using these electrons is based upon the atomic number of the elements and their arrangement. BSE-images are therefore used to analyze the various phases present in the specimen. On the other hand, secondary electrons are the electrons that escape from the surface region of the specimen with low energy and are used mainly in the analyses of fracture surfaces and surface defects.

Elemental analysis is done by using Energy Dispersive Spectroscopy (EDS), a quantitative method which works by analyzing characteristic X-Rays. Characteristic X-Rays are produced when the beam of electrons is incident on the specimen and an electron is knocked off from the inner shell

of the atom leaving the atom in the high energy state. An electron from the outer shell drops down to occupy the vacant position bringing the atom to low energy state. As a result energy in the form of radiation is emitted and is characteristic for that element. For EDS analysis the instrument was calibrated with a homogeneous and stoichiometric (25 at.% Sn) bulk Nb_3Sn sample [41].

In the present work, microanalysis was done with the aid of a QUANTA SEM and a SIRION SEM operating in the back-scatter electron (BSE) mode. Interaction volumes were calculated using Monte Carlo simulations and were kept below 0.85 μm [35, 42]. Microchemical analysis was performed via Energy Dispersive spectroscopy (EDS) at 20 kV and an operating distance of 5 mm on SIRION SEM. Fractography was performed on samples with the aid of a SIRION field emission SEM having a spatial resolution of 2.5 nm at 15 kV operating in the ultra high resolution mode.

After obtaining the BSE images, the Sn, Cu and Nb area fractions were determined using image analysis tools Adobe Photoshop and Image Tool. The BSE images have good atomic number contrast; therefore various phases can easily be differentiated.

CHAPTER 4

INFLUENCE OF LOW TEMPERATURE REACTION HEAT TREATMENT ON THE MICROSTRUCTURE AND PROPERTIES OF TUBE TYPE Nb_3Sn STRANDS

4.1 Introduction

In this chapter the transport and the microstructural properties of Tube-Type Nb_3Sn conductors were studied for strands subjected to lower reaction temperatures, and these results were compared to those obtained at higher reaction temperatures. For this purpose nine different multifilamentary Tube Type composites (as described in Table 3.1) were used. In the first section (Section 4.2) we describe the phase formation as a function of reaction time at these lower temperatures. After this, the focus shifts to the correlation of composition and morphology of the transport and magnetic properties for strands subjected to various lower temperature full reaction heat treatments. Compositional analysis was carried out on the A15 phase to study the variation in stoichiometry as a function of temperature. Fractography was also performed to investigate the influence of temperature

on the morphology the ratio of the coarse/fine grain areas and grain size of the fine grain A15.

4.2 Phase Evolution and Layer Growth of Nb_3Sn in Tube Type Conductors

It was of interest to investigate the phase formation of the Tube samples when they were given lower temperature reaction HTs. In order to do this, the samples (from strand S7) were HT for various times under flowing Ar, and then removed from the oven, with the sequence as described in Table 3.4. Qualitatively, the reaction sequence was quite similar to that at higher temperatures, as shown in Figure 4.1, where we see the morphology for strand S7 heat treated at 635°C at several specific times before complete reaction. In a more comprehensive way, Figure 4.2 shows the Nb_6Sn_5 and A15 growth rates for sample S7 HT at 625°C and 635°C. We have calculated the layer thickness of Nb_6Sn_5 and A15 using an Image Tool (an image processing software) to measure the areas of the annular regions of these phases, and then, assuming a perfect annulus, have extracted the average thickness.

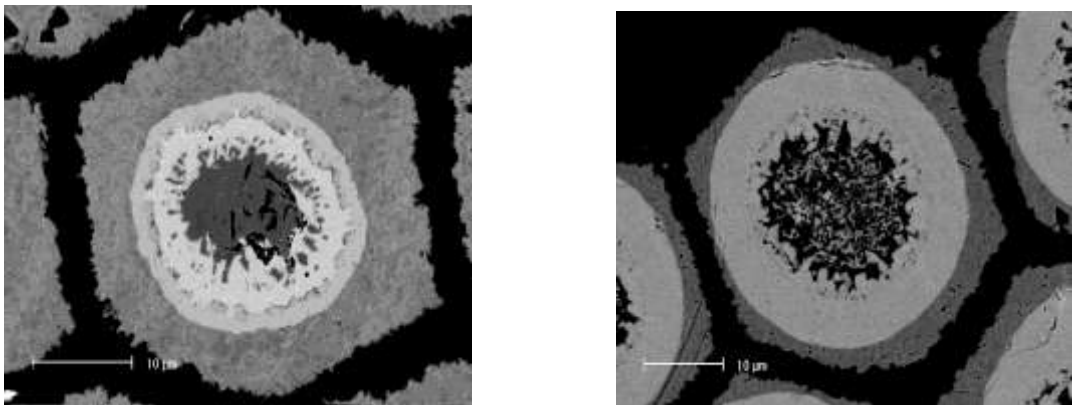

(a) (b)

Fig. 4.1 BSE images of strand S7 HT at 635°C for (a) 12 h (b) 100 h indicating the A15 layer growth.

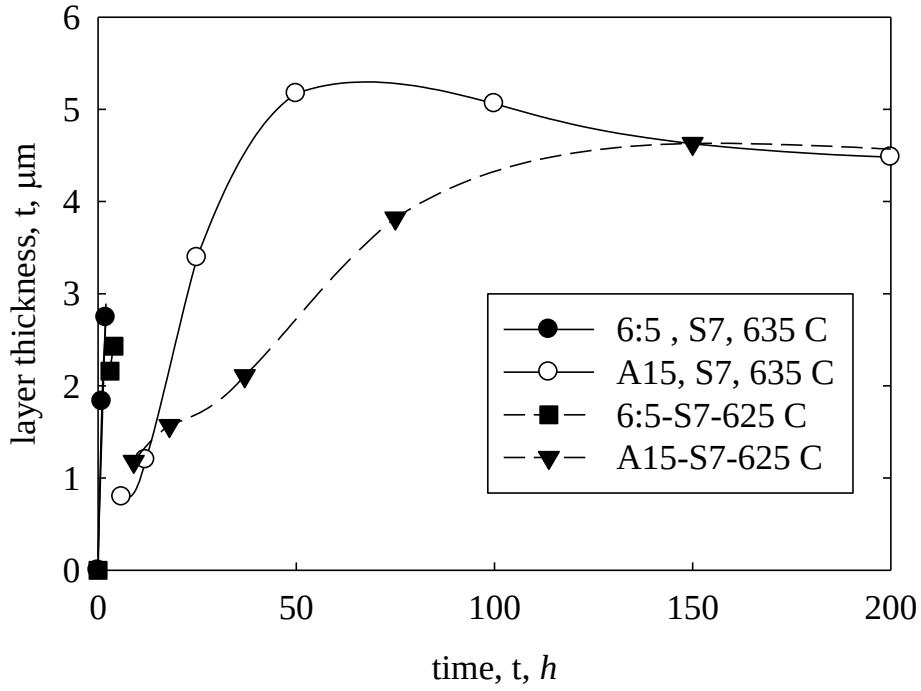

Fig. 4.2 Nb_6Sn_5 (6:5) and A15 growth rate vs time for S7 (Tube Type strand with 217 subelements) at 625°C and 635°C.

These values are displayed in Fig. 4.2. We can see that the Nb_6Sn_5 forms quite rapidly at both 625°C and 635°C, while the A15 growth rate, as expected, is lower at 625°C. However, it can be seen that for the present conductors (0.7 mm with 217 filaments) the growth seems complete at 50 and 150 h at 635°C and 625°C, respectively. On the other hand, the best J_c properties were found for times somewhat longer than this, this may be due a need for additional Sn homogenization.

4.3 Transport Properties of Strands

Moving now to full reaction studies at lower temperatures, Figure 4.3 shows the J_c curves for different Tube Type strands (S6, S7 and S9) given various (full reaction) heat treatments. Sample descriptions and heat treatment schedules for these full reaction studies are given in Table 3.1 and Table 3.5 (upper portion) respectively. Generally, transport J_c values were observed to be higher for lower temperature heat treatments. The best J_c value found in this set was 2440 A/mm^2 at 12 T for sample S6 given a heat treatment of 625°C for 500 h. The reason for this is that lower temperature heat treatment inhibits the grain growth leading to fine grain structure as is well known. The particular temperatures we have used are very low, and the

data represents the first low temperature reaction HT study for Tube Type strands; the details are shown below.

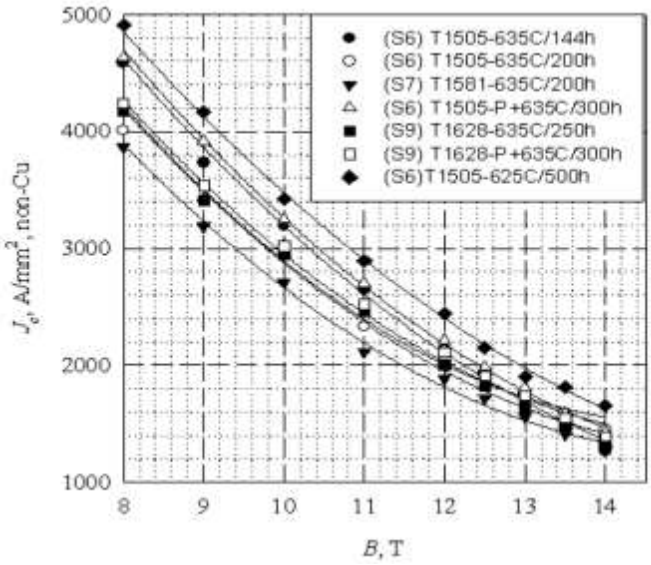

Fig. 4.3 Transport J_c vs B for Tube type strands HT at low temperatures.

As will be shown in later in the Section 4.3, fine and coarse grain size decreases with decreasing temperature with the fine grain size ranging from 80 ± 10 nm to 100 ± 10 nm for various heat treatments at 625°C. As a result, flux pinning is enhanced which increases the critical current density. As noted above, it was necessary to select HTs for the transport studies which were expected to be fully reacted, but not to let the reaction go so long as to allow Sn to diffuse into the Cu matrix. This was because exceptionally long reaction times would allow Sn to diffuse into the matrix making it impossible to measure the transport properties of the strands. It was then of

interest to do a series of samples for electron optics study only, in order to see what the result would be. These results are described below.

4.4 Grain Size Analysis of the Fully Reacted Microstructure

Following the full reaction transport studies of the previous section, it was interesting to see what long time reactions at the temperatures would give. The samples would not be measureable for transport properties, but it would be possible to see what the long time reaction microstrucure was. Thus, a series of strands, S1-S5, where reacted for 1000 h, as described in the lower part of Table 3.5. Figure 4.4 shows a full reaction subelement micrograph of strand S1 heat treated at 625°C for 1000 h. Fracture SEM of typical subelements of strands S1-S5 reacted at 625°C for 1000 h are shown in Fig. 4.5. As has been seen previously [35, 42], coarse grain A15 was found near the inner boundary of the superconducting annulus (close to the Sn source) and fine grain A15 was seen in the outer regions of the annulus.

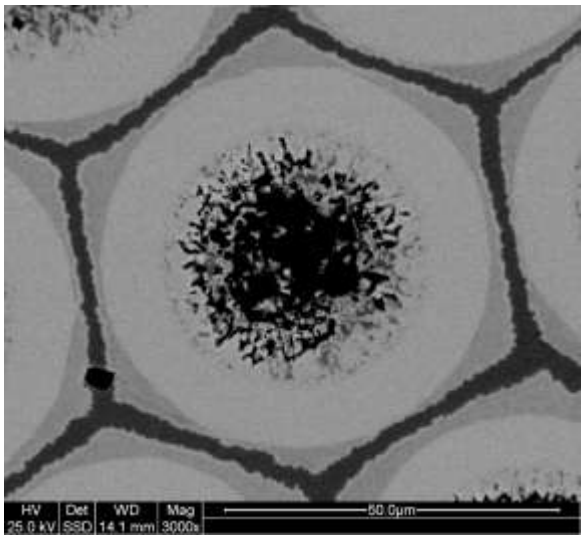

Fig. 4.4 BSE image of reacted subelement S1 HT at 625°C/1000 h shows the full reaction microstructure.

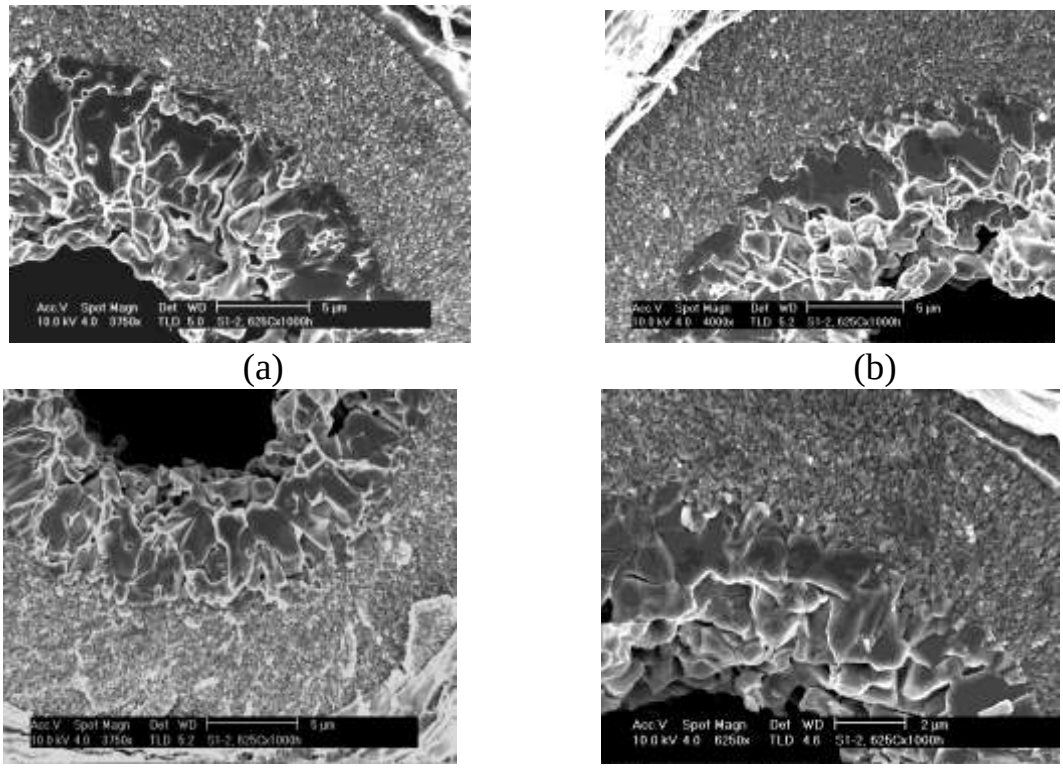

(a) (b)

(c) (d)

Fig. 4.5 Fracture SEM for S1-S4 HT for 625°C/1000 h (a) S1, (b) S2, (c) S3, (d) S4 (shows coarse and fine grain A15).

Table 4.1 summarizes the quantitative analysis performed on the fracture micrographs of strands S1-S5 HT at 625°C for 1000 h. The fine grain A15 region varies from 37% to 46% of the total cross sectional area of the subelement for this strand set. The FG/CG ratio ranges from 1.83 to 2.62, similar to what had been found for strands reacted at higher temperatures [36].

Sample Name	**FG/Total Sub**	**CG/Total Sub**	**FG/CG**	**CG Size (±0.15 μm)**	**FG Size (± 10 nm)**
S1	0.41	0.21	1.93	1.16	80
S2	0.44	0.20	2.24	1.11	80
S3	0.37	0.16	2.29	1.07	80
S4	0.39	0.21	1.83	0.79	100
S5	0.46	0.18	2.62	1.11	80

Table 4.1 Fine/Coarse grain area ratio (FG/CG) and sizes for Tube type samples HT at 625°C/1000 h (see Table 3.5).

High resolution fractographs shown in Fig. 4.6 were used to perform grain size analysis. The line intercept method was used giving average grain sizes for strands S1-S5; the results are shown in Table 4.1. Fine grain sizes varied from 80 ± 10 nm to 100 ± 10 nm, while the coarse grain size was in the micron range.

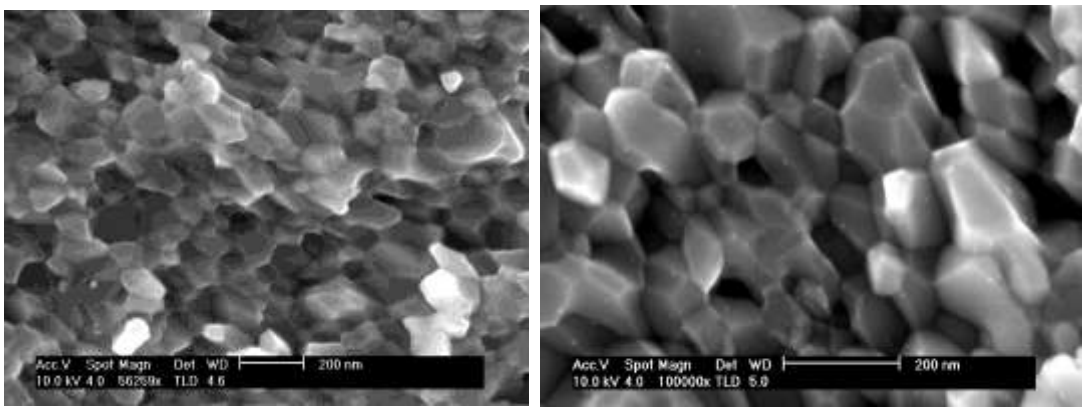

(a) (b)

Fig. 4.6 Fractographs of the fine grain region (a) Strand S4 (b) Strand S4, both heat treated at 625C/1000 h.

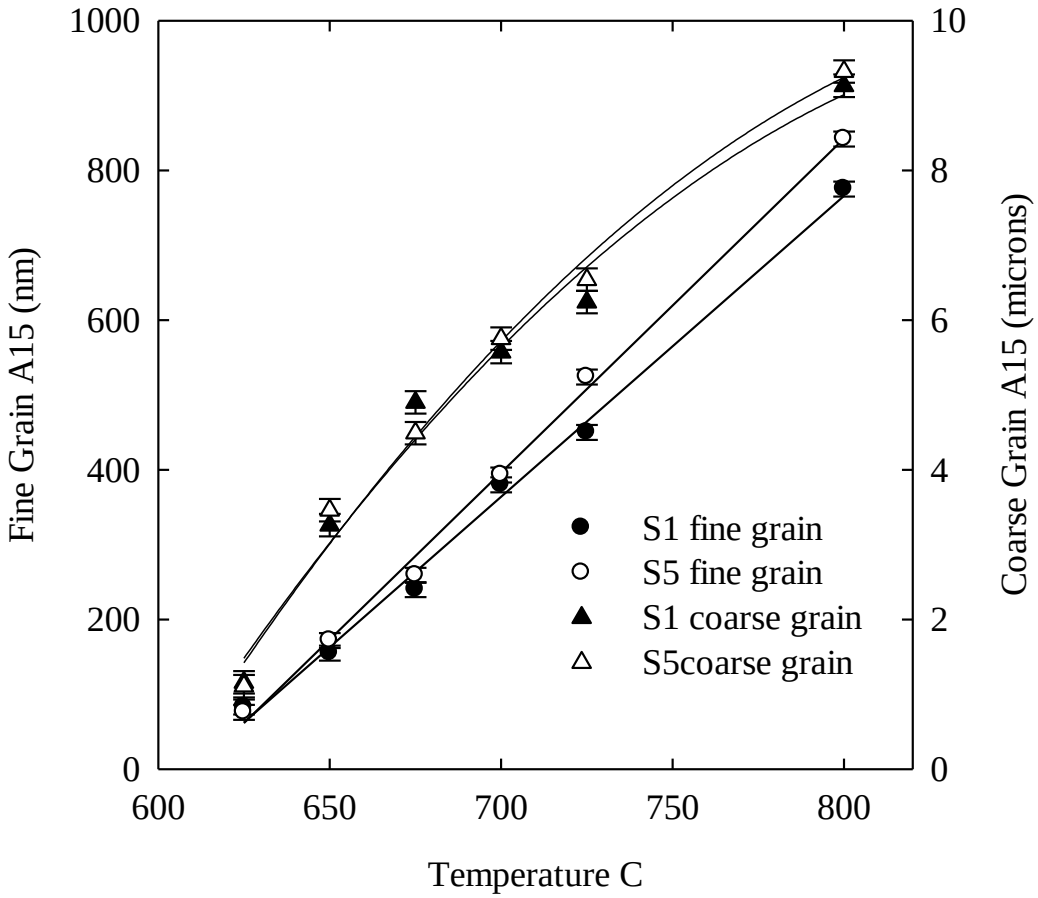

Fig. 4.7 Coarse and Fine grain size vs *T* for S1 (Tube type strand with high Cu content) and S5 (tube type strand with low Cu content), (Includes data from Ref [35, 42] for higher temperature values) showing the variation of grain size with temperature.

As indicated in Fig. 4.7, fine grain size decreases linearly with temperature ranging from 800°C to 625°C for Tube type strands S1 (high Cu content) and S5 (low Cu content). For comparison purposes, Fig. 4.7 displays grain size data from previous measurements [35, 42], the lowest temperature points are new. We can also see in Fig. 4.7 a corresponding decrease with temperature in the coarse grain, which is again attributable to the inhibition of the grain growth kinetics at lower temperature.

Figure 4.8 shows high resolution SEM for the grain structure in samples S6-S8, given the 625°C HTs. Here we can see the relative uniformity and smallness of the grains in the FG region. There are small specks in the figures, these may be artifacts but bear further investigation and clarification.

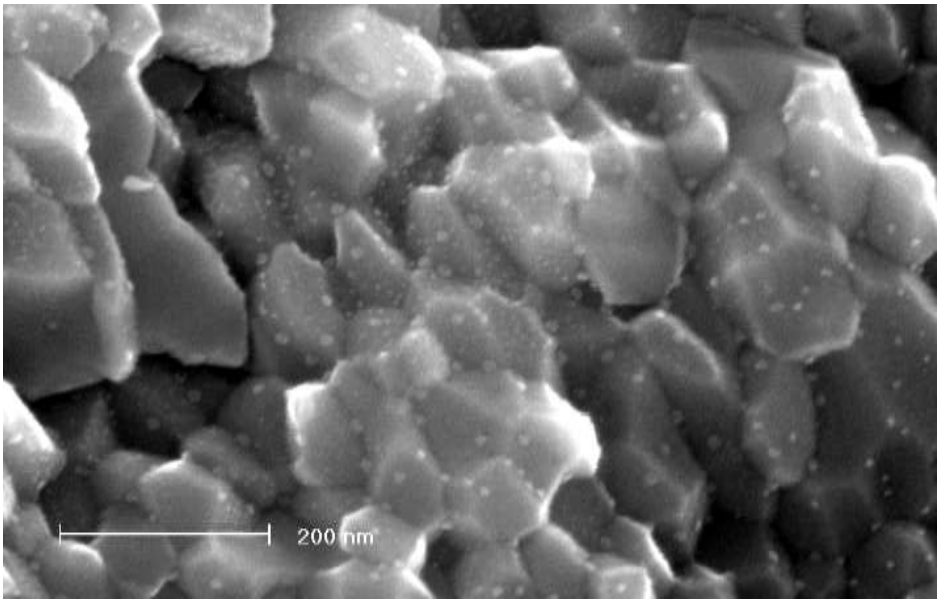

(a)

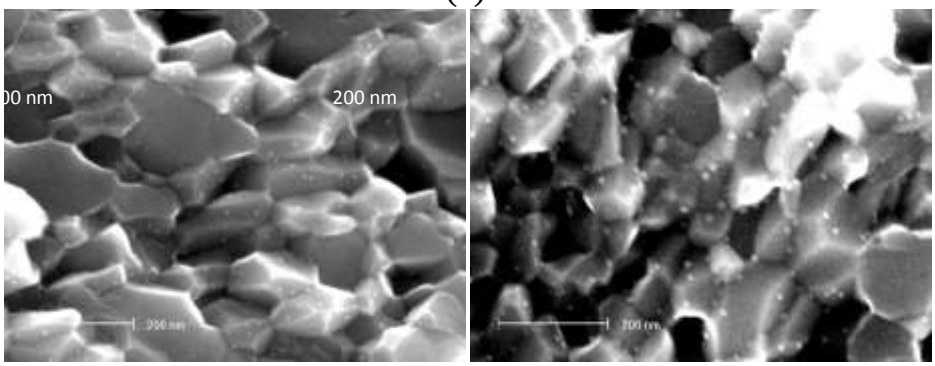

(b) (c)

Fig. 4.8 Fracture SEM of (a) S6, (b) S7, and (c) S8 HT at 625°C, indicating the uniformity of grains in FG region. Small specs may be artifacts.

4.5 Influence of Heat Treatment on the Composition of the A15

Looking further into the results for the fully reacted strands (Table 3.5, bottom), for a few selected samples we observed the composition profiles in the coarse grain (CG) and fine grain (FG) A15 across the filaments. This data was obtained using EDS, with radial distances measured with respect to the coarse-fine grain A15 interface (Fig 4.9 and Fig. 4.10).

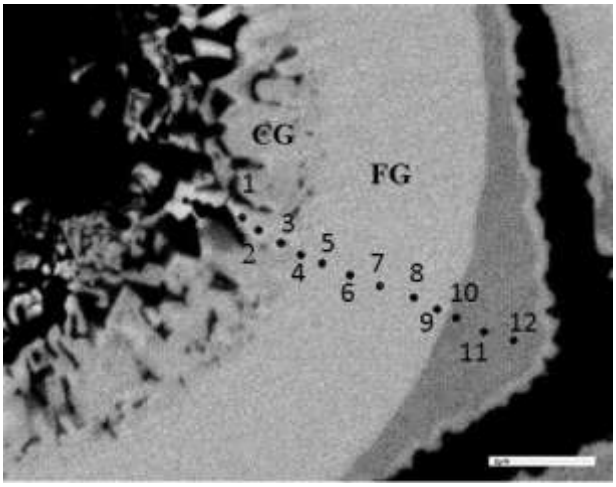

Fig. 4.9 EDS spot scan region for sample S1 HT at 625°C/1000 h, indicating CG and FG region.

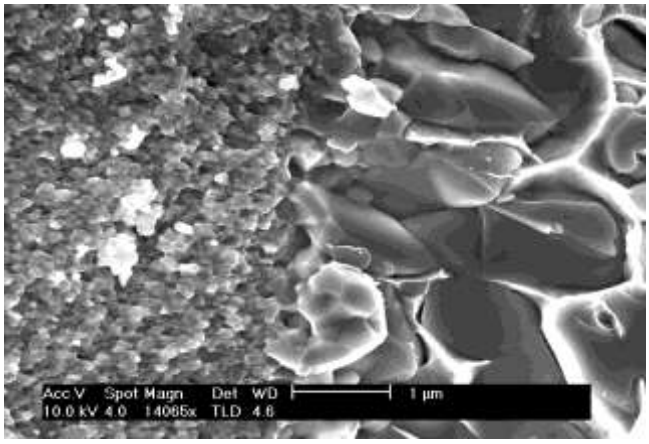

Fig. 4.10 Fracture SEM image of sample S1 HT at 625°C/1000 h, indicating coarse/fine grain interface.

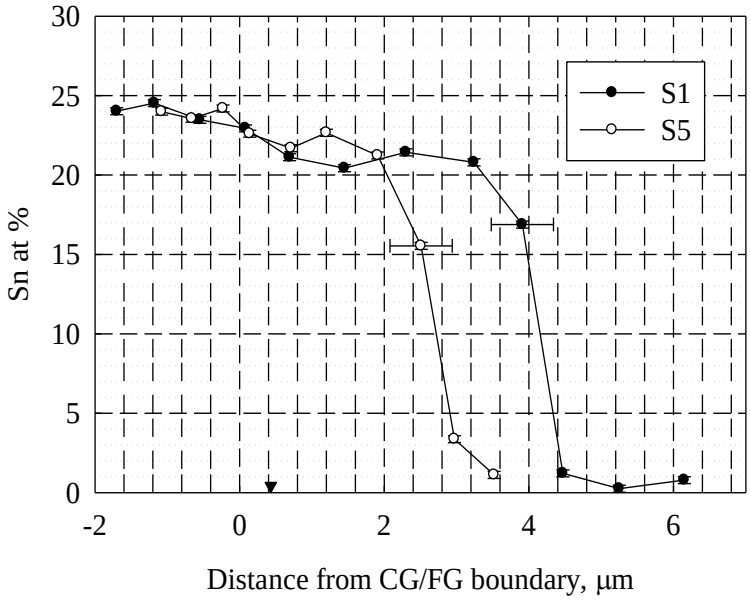

Fig. 4.11 Stoichiometry vs radius for S1 (a Tube type strand with a high Cu content) and S5 (a Tube type strand with low Cu content) HT at 625°C/1000 h. Distances are relative to the CG/FG boundary, with regions on the left nearer the Sn core. The standard deviations show an uncertainty of ±0.22 at.% Sn represented by vertical error bars. Horizontal error bars indicates the spatial resolution of ~ 0.85 μm.

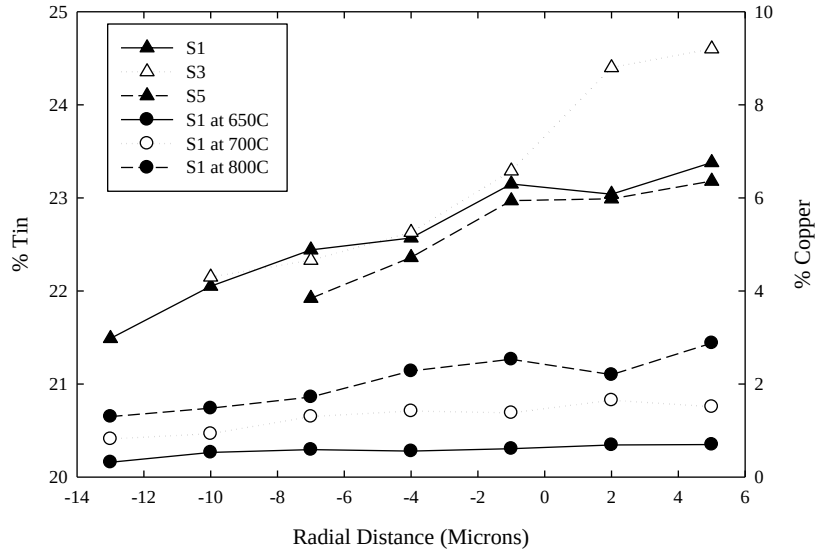

Fig. 4.12 A15 Stoichiometry vs radius for S1 (a Tube Type strand with a high Cu content) and S5 (a Tube Type strand with a low Cu content) at higher temperatures (Reproduced from the work of Vishal Nazareth [35, 42]. Distances are relative to the CG/FG boundary, with regions on the right nearer the Sn core.

Figure 4.11 shows the variation of the Sn content across samples S1 (Tube Type strand with high Cu content) and S5 (Tube Type strand with low Cu content) after complete reaction at 625°C and 1000 h. The Sn content in the coarse grain A15 was found to be 24-25%, and greater than the fine grain A15. Similar behavior was observed at higher temperatures [35, 42] as indicated in Fig 4.12 [35, 42] where the Sn stoichiometry was higher in the coarse grain region compared to fine grain region.

The Sn content was approximately 21-22% in the FG region, with a small Sn gradient observed radially outward. In comparison to results

obtained at higher temperatures [35, 42], Sn content in the FG region was on the lower side. In fact, the coarse grain boundary also exhibited a Sn gradient, which had been less evident at higher temperatures [35, 42].

CHAPTER 5

COMPARISON OF A15 STOICHIOMETRY AND GRAIN MORPHOLOGY IN RIT AND TUBE TYPE STRANDS; INFLUENCE OF STRAND DESIGN, HTs AND DOPING

5.1 Introduction

Previous studies on Nb_3Sn Tube conductors have correlated the initial tin and copper content to the A15 coarse/fine ratios obtained after reaction. Extensive research has been carried out on the variation of grain size and stoichiometry with temperature for Nb_3Sn conductors generally [35, 36, 42, 43], and the same basic trends have held true for Tube type conductors as seen in Chapter 4 and further references [35, 42, 43]. This chapter deals with the detailed investigation of A15 stoichiometry and microstructure for high performance strands, with a direct comparison of the best performing Tube Type and RIT type conductors. A detailed investigation was performed in order to understand the origin of the difference in the transport properties of two strand types. The main focus was on studying key parameters such as A15 stoichiometry, grain size, and the ratio of fine grain/subelement area for both Tube and RIT type strands, and then to correlate these parameters with

the transport properties. Compositional analysis was performed to obtain the A15 stoichiometry for single step heat treatments (samples from Table 3.6) and the results were compared to those for two-step heat treatments (samples from Table 3.7). Fracture SEM was carried out to study the grain morphology of the fine grain A15. The influence of titanium doping on the transport properties of RIT strand was also studied.

5.2 Effect of Heat Treatment on A15 Stoichiometry

This section deals with the investigation of A15 stoichiometry with application of both single and two- step heat treatment to both Tube and RIT type conductors as mentioned in Table 3.6 and 3.7. The first step of the two-step heat treatment was performed at slightly lower temperature than the second step. The aim of the study was to attain fine grain A15 with maximal Sn stoichiometry and homogeneity. The two-step process was mainly aimed at Tube type conductors and was intended to diffuse out to the fine grain A15 the extra Sn found in the core and coarse grain region of these conductors after a standard heat treatment.

Composition profiles were obtained across the Tube type subelement S10 (6.34% Cu in a subelement), with radial distances measured with respect to the coarse-fine grain A15 interface. Figure 5.1 and Fig. 5.2 show the variation in Sn content across strand S10 after reactions using various two-step heat treatments as listed in Table 3.7. The composition profiles across the A15 for various two step heat treatments were found to be similar to those obtained from single-step heat treatments.

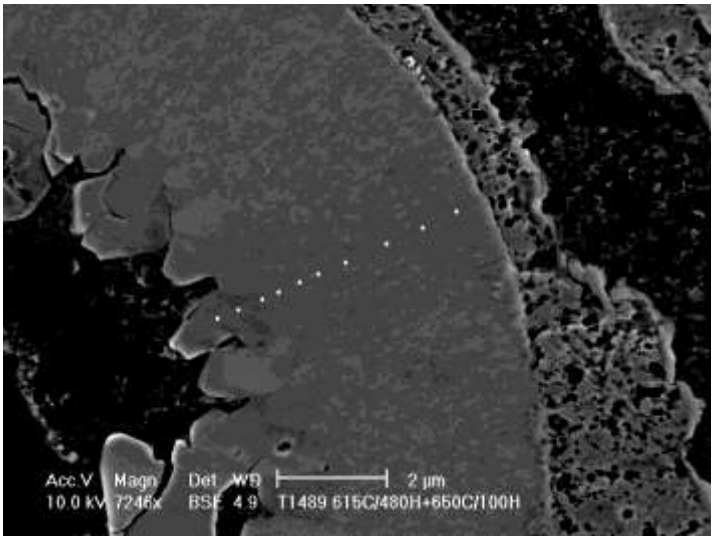

Fig. 5.1 SEM image showing the A15 layer and the locations used for EDS analysis of Tube type strand S10 HT at 615°C for 480 h .

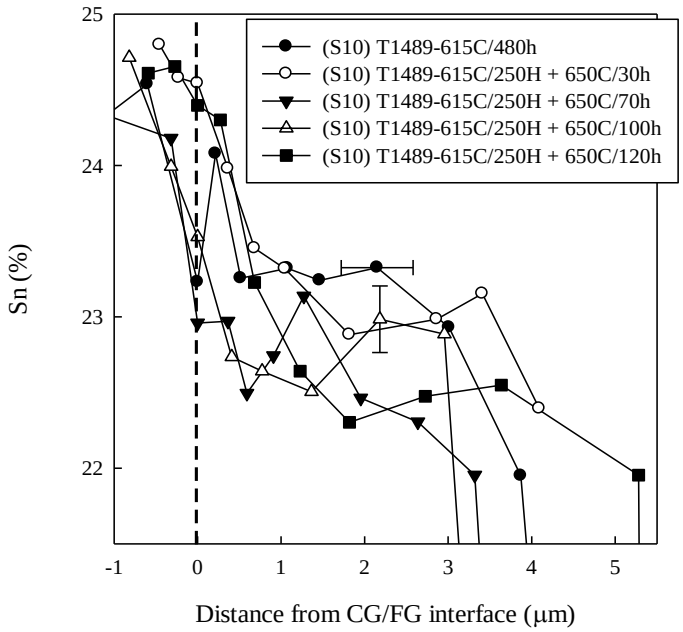

Fig. 5.2 A15 Stoichiometry vs radius for Tube type strand S10 showing the variation of Sn content across the fine and coarse grain A15. Distances are relative to the CG/FG boundary, with regions on the left nearer the Sn core. The standard deviations show an uncertainty of ±0.22 at.% Sn indicated by vertical error bar, horizontal error bars indicates the spatial resolution of ~ 0.85 μm (representative for all points).

As indicated in Table 3.7, a reaction time of 250 h was chosen for step one of the two step heat treatment as compared to 480 h for the single step control sample. Optimization of the time/temperature using a two step heat treatment was pursued in order to enhance the stoichiometry in the A15. The composition profile shows a Sn content of around 23 at.% in the fine grain A15 which is somewhat higher than the previous result at [42, 43].

Figure 5.3 shows the composition profile for sample R1, which is a Rod-In Tube, distributed barrier type conductor. Data is included for both for single and various two step heat treated samples. In comparison with the single step HT results, two step HT samples show similar behaviors with Sn content in A15 ranging from 22.5-23%. Also, the two step HT resulted in composition profiles with lower Sn gradients across A15 region.

A composition profile for RIT strand R2 (which had no Ti doping) heat treated at 650°C for 80 h was also obtained, and shows a Sn content of around 22-22.5 %. In comparison with the results of Tube type conductors, RIT type strands show similar behavior with, A15 stoichiometry ranging from 22-23%.

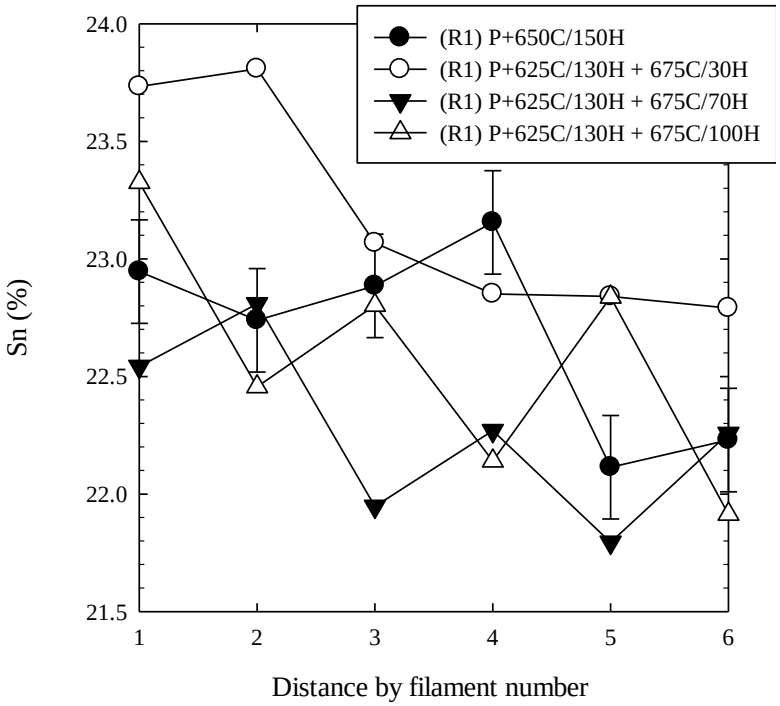

Fig. 5.3 A15 Stoichiometry vs radial distance for RIT strand R1 (without Ti) showing the variation of Sn content across fine grain A15 (regions on the left nearer the Sn core). The standard deviations show an uncertainty of ±0.22 at.% Sn indicated by vertical error bar (representative for all points).

5.3 Grain Size Analysis of the A15

Fractographs of typical subelements of S10 (6.34% Cu in a subelement) are shown in Fig. 5.4 (a) and 5.4 (b) (in this case for a two step heat treatment). Here we can see the relative uniformity and fineness of the grains in the FG region. As has been seen previously, coarse grain A15 is

found near the inner boundary of the superconducting annulus (close to the Sn source) and fine grain A15 is seen in the outer regions of the annulus. Table 5.1 summarizes the grain size analysis which was performed using a line intercept method, giving average grain sizes for tube type strands S6 (4.35% Cu in a subelement) and S10. The FG region grain sizes varied from 80 ± 10 nm to 100 ± 10 nm, while the coarse grain size varied from 0.50 ± 0.20 micron to 1.00 ± 0.20 micron. In comparison with the single step HT, the two-step HT resulted in slightly refined A15 grain sizes.

As indicated in Fig 5.5 coarse grain size decreases linearly with temperature as it drops from 800°C to 615°C which is attributable to the inhibition of the grain growth kinetics at lower temperature. A similar trend was observed in the low temperature studies in Chapter 4. For comparison purposes, Fig 5.5 displays grain size data from previous measurements [35, 42], the lowest temperature points are new. We can also see that FG region grain size may have saturated at the lowest temperature.

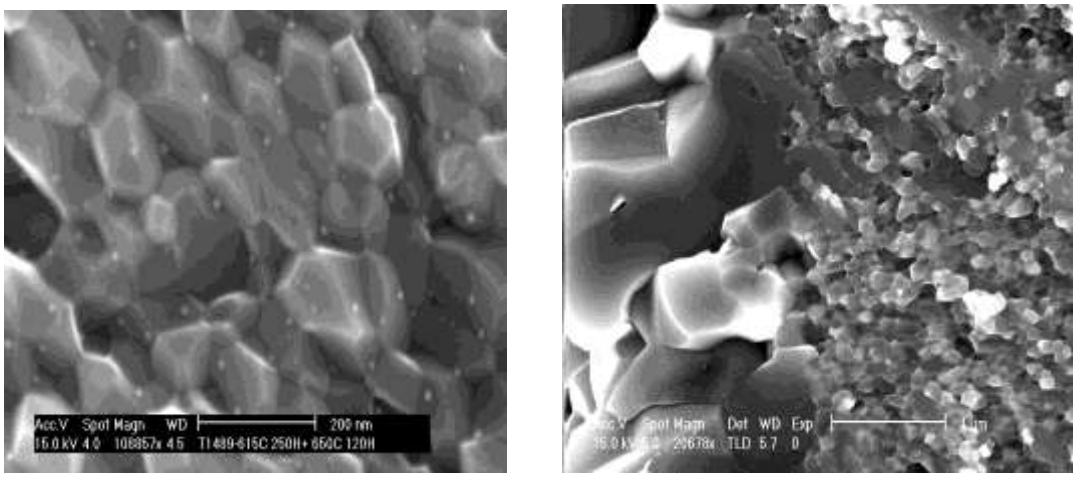

(a) (b)

Fig. 5.4 High resolution fractrograph for the grain structure in samples S10, given a two step HTs showing (a) fine grain A15, and (b) coarse and fine grain.

Strand name	HT(C/h)	FG Size (± 10 nm)	CG Size (± 0.20 μm)
S10	615/480 (control sample)	90	0.69
S10	615/250+650/30	80	0.72
S10	615/250+650/70	75	1.04
S10	615/250+650/100	75	0.54
S10	615/250+650/120	80	0.47
S6	625/500	80	-
S6	635/300	90	-
S9	625/300	95	-

Table 5.1 Grain size analysis for tube type strands for various HTs.

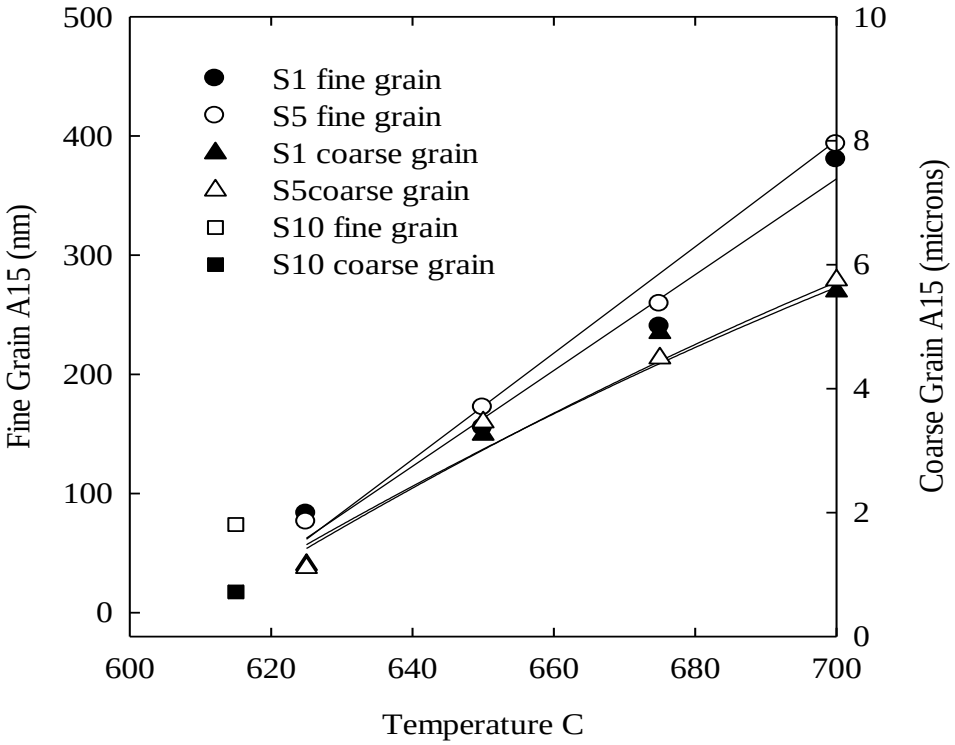

Fig. 5.5 Coarse and fine grain size vs *T* for Tube type strand S10, as compared to data from Ref [35, 42] (for higher temperature values) indicating the variation of grain size with temperature (similar to Figure 4.7 with additional data points for strand S10 HT at 615°C).

Figure 5.6 shows a high resolution fracture micrograph of the grain structure in sample R1 (a RIT without Ti doping), subjected to the two step HT, 625°C for 130 h followed by 675°C for 100 h. Table 5.2 summarizes the grain size for strand R1 for various heat treatments the grain size range from 90 ± 10 nm to 110 ± 10 nm. Fine grain size for the two step HT were on the higher side as compared to single step HT for the RIT strand R1.

In comparing the results obtained for Tube type strands with the RIT type strands, the average grain sizes were observed to be slightly lower for tube type conductors.

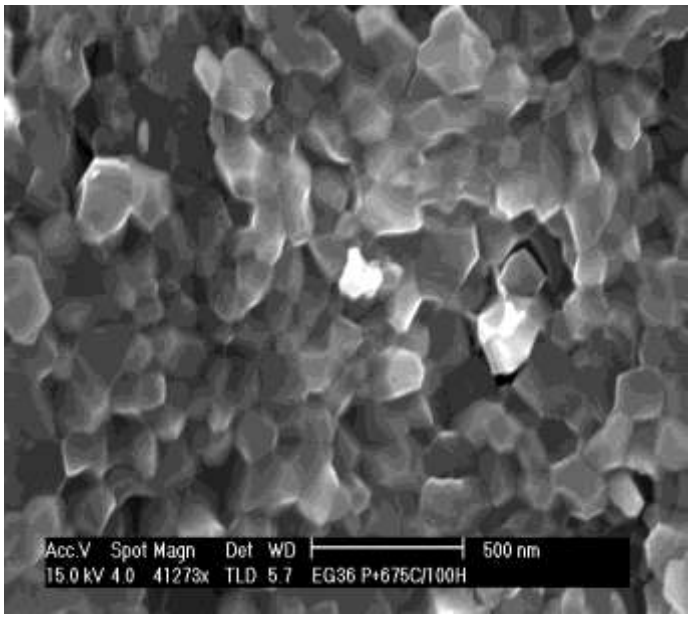

Fig. 5.6 Fractograph for the grain structure in RIT strand R1, given the two step HT.

Strand name	HT (C/h)	Grain size (± 10 nm)
R1	200/72+400/48+650/50	90
R1	P+625/130+675/30	110
R1	P+620/130+675/70	110
R1	P+625/130+675/100	110
GL1	P+650/60	110

Table 5.2 Grain size analysis for RIT strands given various HTs.

5.4 Transport Properties of the Strands

Figure 5.7 shows the J_c curves for the Tube type strand S10 (a 271 subelements strand) for two different heat treatments. A transport J_c value of 2230 A/mm^2 at 12 T was seen for strand S10 reacted at 615°C for 480 h. The two step heat treatment, 615°C for 250 h followed by 650°C for 70 h resulted in a similar (overlapping) J_c curve showing little difference as compared to the single step heat treatment. Transport J_c at 12 T was observed in this latter case to also be 2230 A/mm^2.

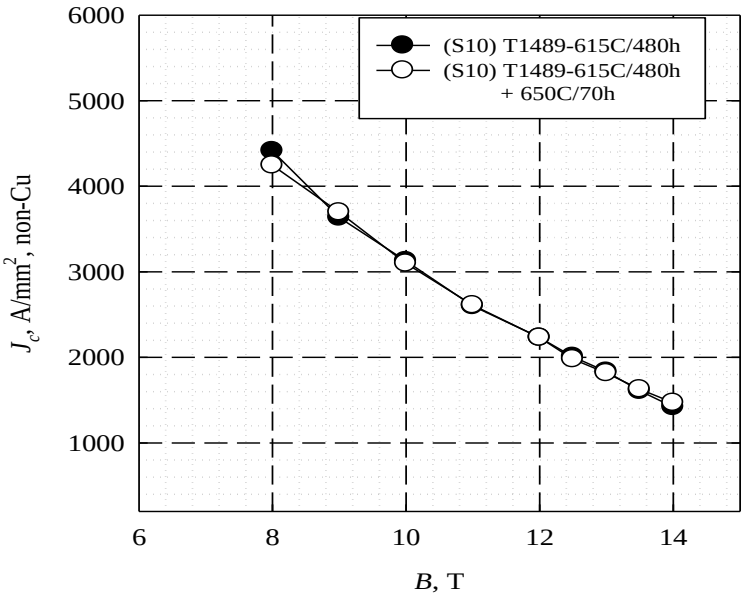

Fig 5.7 Transport J_c vs B plots for tube type strand S10 for single and two-step HTs.

Figure 5.8 shows the J_c curve for RIT strand R1 (91 filament strand) for a single step heat treatment (650°C/50 h). A transport J_c of 3480 A/mm^2 was observed at 12 T.

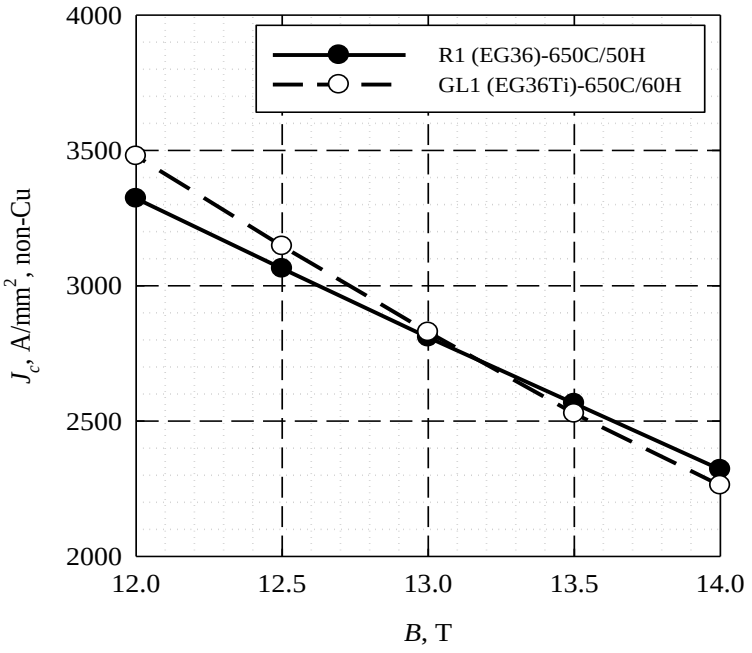

Fig. 5.8 Transport J_c vs B for RIT samples R1(without Ti) and GL1 (with Ti), showing a shallower slope for RIT strands with Ti additions.

Titanium doped sample GL1 (1.2% Ti) heat treated at 650°C and 60 h showed a shallower J_c-B slope, and a transport J_c of 3320 A/mm^2 at 12 T. This may be due to the anticipated increase of B_{c2} and a simultaneous reduction in low field flux pinning due to grain growth, as seen for Ti (previously added to less optimized strands).

5.5 Subelement Area Utilization and Layer J_c of the Strands

Above, we have dealt predominantly with the comparison of the grain sizes, A15 stoichiometries, and transport J_c values for two-step reactions as compared with single step reactions. However, we can also usefully compare the single step HT generated values of these quantities between the Tube Type and the RIT type conductors, as well as to the literature.

Table 5.3 lists the transport J_c values at 12 T and 4.2 K for different Tube type and RIT type strands for various heat treatments. As is clear from the result, the non-Cu J_c values of RIT type strands are higher than those of Tube type conductors. It is of interest to ask the question why. We can look at the single step generated grain sizes and stoichiometries of the A15 phase present in the conductor in order to discover the possible reason for the difference in the J_c.

Strand name	HT (C/h)	12 T J_c, A/mm^2
R1	650/50	3480
R2	650/80	3050
R3	650/40	3740
GL1	650/60	3320
S6	625/500	2440
S6	635/300	2210
S9	625/300	2150
S10	615/480	2230
S10	615/250+650/70	2230

Table 5.3 Transport J_c values for Tube type and RIT type strands

For example, it might be expected that a lower stoichiometry in the A15, or a larger grain size could explain the lower non-Cu J_c value of the Tube type conductors. However, a direct comparison of the results between the two strand types, with the analysis performed on very high J_c strands of RIT conductor (3000-3450 A/mm^2 at 12 T) shows that the fine grain sizes and stoichiometries were very similar between the RIT and Tube type conductors.

The results obtained were also compared with those of previous studies on RIT type conductors [44], as well as PIT conductors [45]. Literature values for the very highest performance RIT samples from study [44] were seen to be 120±10 nm for grain size, and 22-24 at.% Sn for stiochiometry. Literature values for the very highest performance PIT samples from study [45] were seen to be 23 at. % Sn for stiochiometry. These were for strands made by HyperTech Inc. (Columbus) for the RIT and Shaped Metal Innovation (Netherlands) for the PIT strands. This can be compared to the above values of 110±10 nm and 22-23 at.%Sn, for grain size and stiochiometry, respectively, for RIT conductors in the present study. They can also be compared to values of 90±10 nm and 23 at.% Sn for Tube type conductors in the present study. Taken together, this shows a strong

similarity in the grain size and stoichiometry (at given heat treatment) for RIT and PIT strands respectively, when given similar heat treatments. Given these strong similarities in RIT and Tube type conductors, neither grain size nor stoichiometry seems to be responsible for the difference in the transport properties of the two strands types. This leaves us with subelement area utilization as the most likely candidate for the difference.

Below we correlate a detailed area analysis of representatives of both strand types with transport properties in order to assess sublelement area utilization. Table 5.4 shows the area estimation, for both Tube and RIT type conductors. Figure 5.9 and Fig 5.10 shows different regions in the subelement for RIT strand R2 and Tube type strand S10.

Strand name	HT (C/h)	% FG	% Hole	%CG	Res%
R1	650/50	66.7	30.0	--	2.3
R2	650/80	60.4	37.4	--	2.2
R3	650/40	59.0	29.1	--	11.9
GL1	650/60	59.1	24,075	--	10.3
S6	625/500	37.4	11.6	20.7	30.3
S6	P+635/300	37.4	7.9	24.4	30.3
S9	625/300	38.6	15.5	16.4	29.5
S10	615/480	34.3	9.96	22.4	33.3

Table 5.4 Subelement area analysis for Tube and RIT strands.

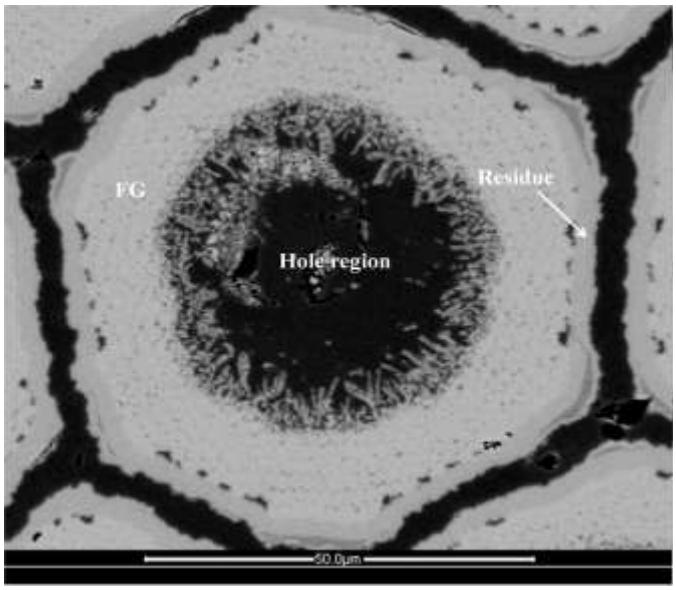

Fig. 5.9 BSE image of RIT strand R2 (without Ti doping) HT at 650°C/80 h indicating different regions of a subelement.

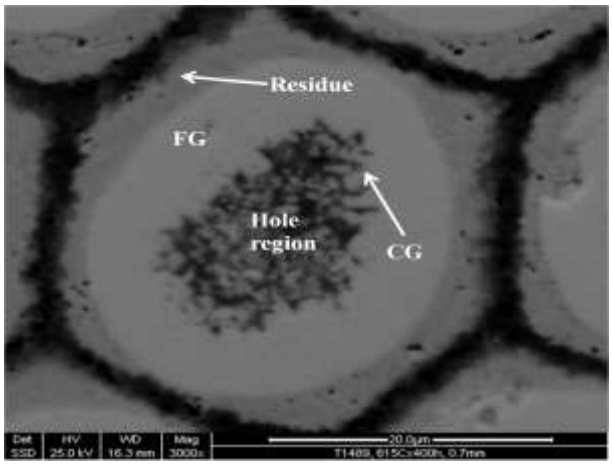

Fig. 5.10 BSE image of Tube type strand S10 (6.34 % Cu in the core) HT at 615°C/480 h indicating different regions of a subelement.

The layer J_c values (listed in Table 5.5) were found to similar for both categories of conductors. In fact, the FG layer J_c values were slightly higher

for Tube type conductors which might be attributed to somewhat lower fine grain size as seen in previous Section 5.4.

Strand name	HT (C/h)	FG Layer J_c 12 T, A/mm^2	Non-Cu J_c 12 T, A/mm^2
R1	650/50	5210	3480
R2	650/80	5040	3050
R3	650/40	4650	3740
GL1	650/60	-	3320
S6	625/500	6100	2440
S6	635/300	5530	2210
S9	625/300	5200	2150
S10	615/480	6070	2230

Table 5.5 FG Layer J_c and non-Cu J_c for RIT strands (R1-R3, GL1) and Tube type strands (S6, S9, S10) for specific HT (FG Layer J_c values corrected for amount of J_c in CG region for Tube type).

As estimated from the subelement area analysis (see Table 5.4), approximately 35-40% of the subelement area in Tube type is utilized for fine grain A15 formation compared to around 60% for RIT strand. Therefore the primary reason for the lower transport properties for Tube type conductors is the insufficient area utilization of the sublement in fine grain A15 formation.

In addition to the above analysis, a comparison of the size of other regions of the subelement (see Fig. 5.9 and Fig. 5.10) including the CG (for Tube type), the central hole or region, and the residual unused area around

the subelement exterior (Res) was also performed (Table 5.4). The result shows that the unreacted Nb-Ta region surrounding the subelements of the Tube type conductors are the biggest contribution to the underutilized area. Of course, both conductor types have unused areas which cause limitations in transport properties, but the outer region of the Tube type conductor stands out as the main determiner of the difference in non-Cu J_c in the Tube and RIT conductors. This is a serious issue for Tube type conductors with around 30% unused subelement area as compared to around 10% for RIT conductors.

A possible solution to this problem could be modification of the strand design for Tube type conductors. The use of round subelement instead of hexagonal could minimize unused area, thereby increasing FG A15 to yield better transport properties.

CHAPTER 6

CONCLUSIONS

In this work the transport and microstructural properties of high performance Tube-Type and RIT type Nb_3Sn conductors were studied under various conditions, with a direct comparison of the both categories of conductors. Various HT were investigated for high performance strands. Transport J_c values for the RIT conductors range from 2750-3470 A/mm^2, as compared to 2000-2440 A/mm^2 for Tube type strands as measured at 12 T and 4.2 K.

One of the main focuses of the work was a study of the transport and microstructural properties of Tube Type Nb_3Sn conductors processed at lower reaction temperatures, comparing to the results obtained at higher reaction temperatures. The lower reactions temperatures used (625°C and 635°C), decreased the grain size and increased the J_cs for these conductors. The best transport J_c value obtained for a Tube Type conductor was 2440/mm^2 at 12 T and 4.2 K on a 217 subelement strand. The stoichiometry

values in the fine grain regions were slightly lower than those for samples reacted with higher temperature reactions. On the other hand, the grain sizes in the fine grain regions were reduced to 80 ± 10 nm to 100 ± 10 nm, while the coarse grain size was reduced to the 1 μm range. On balance, this increased the final transport values to some of the highest seen so far in Tube Type Nb_3Sn. Layer growth rate studies indicated that reactions were complete for reactions times of 50 or 100 h for HT of 635°C and 625°C, respectively. For the present transport samples, somewhat longer times were used indicating further optimizations may be possible.

This work also looked at the results of two step heat reaction HTs treatments for both Tube and RIT conductors, comparing them to single step HTs. The motivation was to utilize the unused Sn at the core and in the coarse grain region of the Tube conductors. However, results for both conductor types were not very different from those of single step heat treatments. Measurements on RIT strands were also included both with low temperature reactions. These HT gave record J_c values for RIT conductors (3480 A/mm^2). Also for RIT conductors near this optimum, titanium doping was investigated. As expected, the results showed a shallower J_c-B slope.

For the optimized strands, the A15 grain size and stoichiometry values in the fine grain A15 were approximately similar for both Tube and RIT conductors. Grain sizes in the FG region were also similar. A more detailed analysis shows that the layer J_c for the tube conductors is similar to that of the RIT conductors. The layer J_c for Tube conductors is 6100 A/mm^2, while that for RIT conductors is 5210 A/mm^2. This is true even though the non-Cu J_c is 2440 A/mm^2 for the Tube conductors and 3480 A/mm^2 for the RIT conductors.

Thus, the primary reason for the lower transport properties for Tube type conductors is the insufficient area utilization of the sublement in fine grain A15 formation (about 60% of RIT used for FG-A15, 35-40% of Tube used for FG-A15). The possible solution to this problem could be the use of round filaments for Tube type conductors, resulting in higher FG A15 region thereby improving non-Cu transport J_c of the material.

REFERENCES

[1] B.T. Matthias, T.H. Geballe, S. Gellar and E. Corenzwit, *Phys. Rev*. **95,** 1435 (1954).

[2] G.F. Hardy and J.K. Hulm, *Phys. Rev*. **89,** 884 (1953).

[3] M. Suenaga, D.O. Welch, R.L. Sabatini, O.F. Kammerer and S. Okuda, *J. Appl. Phys.*, **59** (3), 840 (1986).

[4] R.L. Cooper, *RCA Rev*., **25**, 405 (1964).

[5] H. Hillman and K.J. Best, *IEEE Trans. Mag.*, **13** (5), 1568 (1977).

[6] P.H. Bellin, V. Sadagopan and H.D. Gatos, *J. Appl. Phys*., **40** (10), 3982 (1969).

[7] J.A. Parrell, M.B. Field, Y. Zhang and S. Hong, "*Nb_3Sn Conductor Development for Fusion and Particle Accelerator Applications", Adv. Cryo. Eng. (Materials)* **50B**, 369 (2004).

[8] P. J. Lee, C. M. Fischer, M. T. Naus, M. C. Jewell, A. A. Squitieri, and D. C. Larbalestier, *IEEE Trans. Appl. Supercond.*, **13**, 3422-3425 (2003).

[9] R. M. Scanlan, *IEEE Trans. Appl. Supercond.*, **11**, 2150-2155 (2001).

[10] H. Kamerlingh Onnes, *Leiden Commun*. **124C** (1911).

[11] T.P. Orlando, E.J. McNiff Jr., S. Foner and M.R. Beasley, *Phys. Rev. B*, **19** (9), 4545 (1979).

[12] E.J . Kramer, *J. Appl. Phys*. **44**, 1360 (1973).

[13] C.M. Fisher, "*Investigation of the Relationships Between Superconducting Properties and Nb_3Sn Reaction Conditions in Powder-in-Tube Nb_3Sn Conductors"*, M.S. Thesis, Uni. of Wisconsin, Madison WI, USA (2002).

[14] L. D. Cooley, P.J. Lee and D.C. Larbalestier, "*Changes in Flux Pinning Curve Shape Change for Flux Line Separations Comparable to Grain Size in Nb_3Sn Wires", Adv. Cryog. Eng. (Materials)* **48B**, 925 (2002).

[15] D. Dew-Hughes, *Phil. Mag.* **30**, 293 (1974).

[16] R.M. Scanlan, W.A. Fietz and E.F. Koch, "*Flux Pinning Centers in Superconducting Nb_3Sn", J. Appl. Phys*. **46**, 2244-2249 (1975).

[17] B.J. Shaw, *J. Appl. Phys.* **47,** 2143 (1976).

[18] K.R. Marken, "*Characterization Studies of Bronze-Process Filamentary Nb_3Sn Composites"*, Ph.D. Thesis, University of Wisconsin-Madison (1986).

[19] W. Schauer and W. Schelb, *IEEE Trans. Magn*. **17**, 374 (1981).

[20] A.W. West and R.D. Rawlings, *J. Mat. Sci.* **12**, 1862 (1977).

[21] C.E. Bruzek, P. Sulten, E. Sirot, C. Kohler, P. Mocaer, F. Peltier and G. Grunblatt, *"Effect of Heat Treatments on Superconducting Properties of Nb_3Sn Strands Developed at GEC ALSTHOM", IEEE Trans. Appl. Supercond.*, **7** (2), 1041-1044 (2001).

[22] A. Godeke, *"Performance Boundaries in Nb_3Sn Superconductors"*, PhD. Thesis, University of Twente (2005).

[23] H. Devantay, J. L. Jorda, M. Nindel, B. Obst and R. Flukinger, *J. Mat. Sci.*, **16**, 2145-2153 (1981).

[24] J. P. Charlesworth, I. MacPhail, and P. E. Madsen, *J. of Mat. Sci.*, **5**, 580 (1970).

[25] H. Okamoto , *J. Phase Equilib*., **24**, 380 (2003)

[26] C. Toffolon, C. Servant, J.C. Gachon, and B. Sundman, *J. Phase Equilib*., **23**, 134-139 (2002)

[27] J. J. Hanak, K. Strater, and G. W. Cullen, "*Preparation and Properties of Vapor Deposited Niobium Stannide", RCA (Radio Corporation of America) Review(U.S.)*, **25**, 342, (1964).

[28] M. Suenaga and W. Jansen, *Appl. Phys. Lett*. **43**, 791 (1983).

[29] M. Suenaga, C.J. Klamut, N. Higuchi and T. Kuroda, *IEEE Trans. Mag*., **21**, 305-308 (1985).

[30] A. R. Kaufmann and J. J. Pickett, *Bulletin American Phys. Society*, **15**, 838 (1970).

[31] Y. Hashimoto, K. Yoshizaki and M. Tanaka, *Proc. 5th International Cryogenic Eng. Conf.*, Kyoto, Japan, 332 (1974).

[32] J.D. Elen, C.A.M van Beijen and C.A.M. van der Klein, *IEEE Trans. Mag.*, **13**, 470 (1977).

[33] X. Wu, X. Peng, M.D. Sumption, E. Gregory, M. Tomsic and E. W. Collings, "*Titanium Diffusion and Phase Formation in Tube Type and Rod-In-Tube Type and Internal Sn Nb_3Sn Strands"*, *Adv. Cryo. Eng*., **52**, 504 (2006).

[34] E. Barzi, and S. Mattafarri, *IEEE Trans. Appl. Supercond*., **13**, 3414-3417 (2003).

[35] V.R. Nazareth, M.D. Sumption, X. Peng, E. Gregory, M. Tomsic, and E.W. Collings, *Adv. Cryo. Eng*., **54**, 260-268 (2008).

[36] V.R. Nazareth, M.D. Sumption, X. Peng, E. Gregory, M. Tomsic, E.W. Collings, *IEEE Trans. Appl. Supercond*., **18**, 1005 – 1009 (2008).

[37] S. Murase, M. Koizumi, O.Horigami, H. Shiraki, Y.Koike, E.Suzuki, M. Ichihara, M. Nakane, and N. Aoki, *"Multifilament Niobium-Tin Conductors"*, *IEEE Trans on Magnetics*. **15,** 83-86 (1979).

[38] D. Rodrigues Jr. and J. P. B. Machado, *Materials Research*, **3**, 99-103 (2000).

[39] H. Yamasaki, M. Umeda, M. Watanabe and Y. Kimura, *J. Appl. Phys*., **53**, 7479-85 (1982).

[40] H. Yamasaki and Y. Kimura, *Cryogenics*, **22**, 89-94 (1982).

[41] W. Goldacker, R. Ahrens, M. Nindel, B. Obst, and C. Meingast, *"HIP synthesized Nb_3Sn bulk materials with extraordinary homogeneity"*, *IEEE Trans. Appl. Supercond.*, **3**, 1322-1325 (1993).

[42] V.R. Nazareth, *"Characterization of the Inter Diffusion Microstructure, A15 Layer growth and Stoichiometry in Tube-Type Nb_3Sn Composites",* MS Thesis, Ohio State University (2008).

[43] S. Bhartiya, M.D. Sumption, X. Peng, E. Gregory, M. Tomsic and E.W. Collings, *IEEE Trans. Appl. Supercond.*, **19**, 2588-2592 (2009).

[44] P. Lee and D. Larbalestier, *IEEE Trans. Appl. Supercond.*, **15**, No. 2, 2 (2005)

[45] A. Godeke et al., *Cryogenics*, **48**, 308-316 (2007)